Mixing in the North Atlantic Tracer Release Experiment: Observations and Numerical Simulations of Lagrangian Particles and Passive Tracer

by

Miles Aaron Sundermeyer

B.A. University of California, Santa Cruz,
(1991)

Submitted in partial fulfillment of the
requirements for the degree of

MASTER OF SCIENCE

at the

MASSACHUSETTS INSTITUTE OF TECHNOLOGY

and the

WOODS HOLE OCEANOGRAPHIC INSTITUTION

September 1995

© Miles Aaron Sundermeyer 1995

Signature of Author..
Joint Program in Physical Oceanography
Massachusetts Institute of Technology
Woods Hole Oceanographic Institution
July 31, 1995

Certified by...
James F. Price
Senior Scientist
Thesis Supervisor

Accepted by ....
Carl Wunsch
Chairman, Joint Committee for Physical Oceanography
Massachusetts Institute of Technology
Woods Hole Oceanographic Institution

Mixing in the North Atlantic Tracer Release Experiment: Observations and Numerical Simulations of Lagrangian Particles and Passive Tracer

by

Miles Aaron Sundermeyer

Abstract

Mixing and stirring of passive tracer and Lagrangian particles in the open ocean was studied through comparison of observations from the North Atlantic Tracer Release Experiment, a numerical model, and existing theory. Based on the observed distribution of tracer during the first six months of the NATRE field experiment, Ledwell *et al.* (1993) estimated that on scales of 1 to 10 km small-scale diffusivity $\kappa_s \approx 3$ m^{2}s^{-1} and rms strain rate $\gamma \approx 3 \times 10^{-7}$ s^{-1}. From the observed tracer distribution after one year, Ledwell (personal communication) further estimated that on scales greater than the mesoscale the effective eddy diffusivity $\kappa_e \approx 1 \times 10^3$ m^{2}s^{-1}. In the present study, statistics of the NATRE float data and numerical simulations of Lagrangian particles and passive tracer were used to determine the biases and uncertainties associated with these estimates. The numerical model was calibrated so that the statistics of model floats agreed as closely as possible with the NATRE floats. It is found that observations of a passive tracer such as were made during the NATRE experiment may be used to determine the rms streak width, σ_s, and the rms strain rate and hence to estimate the effective small-scale diffusivity. However, caution must be exercised when estimating κ_s from the theoretical balance, $\sigma_s = \sqrt{\kappa_s/\gamma}$, as this may introduce a bias which would lead to the over-estimation of κ_s. Of particular relevance to NATRE is that observations of σ_s may be biased toward larger estimated rms streak width due to the inability of the observer to distinguish individual streaks from those which have resulted from a recent merger of streaks. Numerical experiments show that such a bias could lead to the over-estimation of κ_s by up to a factor of 2 to 4, suggesting that the estimate of κ_s made by Ledwell *et al.*, (1993) from the NATRE tracer observations has an associated uncertainty of similar magnitude. Analysis of NATRE float data indicates that the estimate $\kappa_e \approx 1 \times 10^3$ m^{2}s^{-1} inferred from the tracer distribution in Spring, 1993 and Fall, 1994 is accurate to within a factor of 2.

Thesis Supervisor: James F. Price
Title: Senior Scientist

Acknowledgements

I am grateful to my advisor, Jim Price, for his continuous support and helpful advice through the highs and the lows of my first few years in the Joint Program. My thesis committee members, Glenn Flierl, Phil Richardson, John Toole, and especially Jim Ledwell also provided many useful suggestions for this work during the past year.

Jim Ledwell was kind enough to give me access to the tracer data collected by him and Andy Watson. Thanks also to Nancy Brink and Bob Weller for sneak previews of their Subduction mooring data report.

The numerical model by Glenn Flierl and Bill Dewar was indispensable in this work, as was the advice of Glenn. Audrey Rogerson provided numerous useful discussions and bits and pieces of code as well, and along with Joe Lacasce saved me many frustrating hours (and gray hairs) in front of the computer and in my analysis.

My appreciation is also extended to my thesis committee members, and to Dave Chapman and Paola Rizzoli for giving me the opportunity to orally defend my Masters thesis and for their comments on the written document. Audrey Rogerson, Natalia Beliakova, Derek Fong, Lyn Harris, and Bonnie Ripley also provided many useful comments on the written thesis. I especially thank Bonnie for all the hours of painstaking editing and moral support.

Finally, my sincerest thanks to my parents and to my siblings for their love and encouragement, and for impressing upon me that I can achieve anything that I set out to do.

Contents

Chapter 1

Stirring and Mixing in a Turbulent Ocean

1.1   The Point Release of a Passive Tracer

The dispersal of dynamically passive tracers and suspended materials in the ocean is of practical importance to understanding the distribution of natural and anthropogenic pollutants, nutrients, and planktonic organisms. Classical theory is well equipped to predict the rate of tracer dispersal in the presence of a purely diffusive and laminar advective process. However, with the inclusion of turbulent shearing and straining, as must occur in the ocean, the result is not so readily predicted. A number of theoretical and numerical studies have investigated the spreading of tracer as it is diffused and stirred by motion at different scales. Young, Rhines and Garrett (1982) estimated the effective small-scale horizontal dispersion which results from the interaction between vertical shear due to internal waves and an ambient vertical diffusivity. Garrett (1983) used this result to arrive at a theoretical prediction for the rate of tracer dispersal as the size of the patch evolves from the sub-mesoscale to scales large compared to the mesoscale. Haidvogel and Keffer (1984) used numerical simulations to examine the combined effects of stirring and mixing processes on a passive tracer in terms of the evolution of tracer concentration, spatial gradients and variance. Numerical investigations of passive tracer (and limited Lagrangian particle) dynamics have also been carried out by Holloway and Kristmannsson (1987), who examined higher moments of tracer. These studies have shown that the rate of tracer dispersal can

be significantly enhanced by turbulent stirring. However, these theoretical and numerical studies of stirring and mixing have seen little confirmation by oceanic observations.

The North Atlantic Tracer Release Experiment (NATRE) provides unique observations of the controlled release and subsequent dispersal of a passive tracer and Lagrangian particles for typical open-ocean conditions. Based on the observed distribution of tracer during the NATRE field experiment, Ledwell $et\ al.$ (1993) estimated that on scales of $1-10$ km the rms strain rate, $\gamma \approx 3 \times 10^{-7}$ s^{-1}, and small-scale diffusivity, $\kappa_s \approx 3$ m^{2}s^{-1}. Ledwell (personal communication) further estimated that on scales greater than the mesoscale the effective eddy diffusivity, $\kappa_e \approx 1 \times 10^3$ m^{2}s^{-1}. In the present study, I examine the statistics of the NATRE float data, and use a numerical model to estimate the biases and uncertainties associated with these estimates. The broad goal is to better characterize isopycnal mixing and stirring of passive tracer in the open ocean. Within the scope of this objective lies the question of whether the dispersion of passive tracer observed in NATRE is well described by the theoretical framework outlined by Garrett (1983). Also addressed is whether the advection and diffusion of Lagrangian particles and passive tracer in the open ocean are well described and predicted (in a statistical sense) by the barotropic vorticity models which have traditionally been used to study this problem.

In the remainder of this chapter, the statistical tools for quantifying the dispersal and diffusion of Lagrangian particles and passive tracer are defined (readers familiar with Garrett (1983) and Taylor (1921) may skip this material). Chapter 2 provides an overview of the NATRE experiment, along with a statistical description of the observed tracer and float dispersal. These statistics are then compared with classical theoretical predictions for tracer area and concentration, and for dispersal rates in homogeneous turbulent flows. Chapter 3 introduces a numerical two-dimensional vorticity model which is used to simulate tracer and float dispersal. The "calibration" of the model against NATRE float observations is explained, and a description of model Lagrangian particle statistics for a "standard" model run is given. Also in chapter 3, the qualitative agreement between model and observed tracer is discussed, as are the biases and uncertainties associated with using the theoretical relationship, $\sigma_s = \sqrt{\kappa_s/\gamma}$, to estimate the small-scale diffusivity, κ_s. Finally, chapter 4 provides a discussion of the implications to estimates of effective small-scale diffusivity and the effective eddy diffusivity, κ_e, made from the NATRE field observations.

1.2 Theories of Tracer Dispersal

Theoretical predictions for the dispersion of a point release of passive tracer in the presence of both mixing and stirring processes are reviewed. These predictions are used in chapter 2 to examine the tracer observations from NATRE and in chapter 3 in the analysis of numerical results. In all of this, it is assumed the ocean is horizontally homogeneous and statistically stationary on the scales of interest.

For an initially localized concentration of passive tracer into the ocean, two different types of processes may be distinguished which act to disperse the tracer. The first are diffusive or "mixing" processes which act to reduce tracer gradients. The second are "stirring" processes which tend to sharpen tracer gradients (Eckart, 1948). Put another way, "mixing" processes are those which can be (or must be) modeled by Fickian diffusion, e.g., molecular diffusion or sub-gridscale processes in which individual exchange events are not resolved, while "stirring" processes are resolved exchange events, e.g., the streaking and folding of tracer within a resolved eddy field. The distinction between these two types of processes is in practice one of scale separation, i.e. small verses large scale, or, in a modeling context, sub-gridscale verses resolved motions.

1.2.1 Dispersion for Small and Large Scale Processes

In the open ocean, horizontal dispersion is believed to be dominated on the small scale by effective horizontal diffusion or mixing due to the interaction between vertical diffusion and vertical shear due to internal waves (Young et al., 1982). On large scales, however, the dominant process is straining or stirring due to mesoscale eddies (Garrett, 1983). One of the primary differences between these processes is the horizontal scales at which they prevail. Consider a very localized region (a point release) in the open ocean which has been injected with some specified amount, M, of passive tracer. The subsequent dispersal of tracer may be modeled as occurring in three distinct stages (Garrett, 1983), as follows.

Stage One: Initially, the rate of dispersion is dominated by an effective small-scale diffusion, κ_s, caused by internal and inertial waves acting on horizontal scales of less than a few kilometers (Young et al., 1982). Based on existing theories of diffusion (e.g., Fisher et al., 1979), the radius of the domain occupied by 95% of the tracer grows as $2\sigma = 2\sqrt{2\kappa_s t}$,

where σ is the standard deviation. This can be used to define an approximate horizontal area occupied by the tracer,

$$A_s = 8\pi\kappa_s t, \tag{1.1}$$

and an associated mean tracer concentration within this radius,

$$C_s = \frac{M}{8\pi\kappa_s t}. \tag{1.2}$$

Young *et al.* (1982) estimate that the effective small-scale diffusivity, κ_s, due to shear dispersion by inertial and internal waves is typically $\kappa_s \approx 10^{-2}$ m^{2}s^{-1} in the open ocean.

Stage Two: As the patch grows, it eventually reaches a transition scale, L_s, where horizontal stirring due to geostrophic eddies begins to significantly strain the tracer into streaks (this stage of the dispersal process is described in detail by Garrett, 1983). For a diffusivity, κ_s, and a mesoscale strain rate, $\gamma = \overline{(u_x^2 + v_y^2)}^{\frac{1}{2}}$, the predicted transition scale is $L_s = \sqrt{\kappa_s/\gamma}$. Taking typical oceanic values of $\kappa_s \approx 10^{-2}$ m^{2}s^{-1} and $\gamma \approx 10^{-6}$ s^{-1} (Young *et al.*, 1982), this transition scale is $L_s \approx 100$ m. Garrett (1983) further estimated that the time when this occurs is $(4\gamma)^{-1}$, which for the above γ is about 3 days. As this scale is reached, this theory predicts that tracer streaks will be elongated at a rate proportional to γ. In the presence of a pure strain field, the streak length L is expected to grow exponentially, at a rate $L = L_s e^{\alpha\gamma t}$, where α is an order-one coefficient. During this second stage of dispersal the mesoscale straining tends to elongate or stir the tracer into thinner streaks, thus increasing tracer gradients, while small-scale diffusion or mixing acts to widen the streaks and smooth tracer gradients. Simple scaling arguments suggest there will be an approximate balance between these two opposing tendencies such that the tracer distribution will achieve a steady rms streak width characterized by a standard deviation $\sigma = \sqrt{\kappa_s/\gamma}$. Based on these predictions for the length and width of the streaks, Garrett (1983) estimated the area stained by the tracer during this stage of the dispersal process grows as

$$A_t = \pi \left(\frac{\kappa_s}{\gamma}\right) e^{\left[\alpha\gamma\left(t - \frac{1}{4\gamma}\right)\right]}, \tag{1.3}$$

and the concentration decreases as

$$C_t = \frac{M}{A_t} = \frac{M}{\pi}\left(\frac{\gamma}{\kappa_s}\right) e^{-\left[\alpha\gamma\left(t - \frac{1}{4\gamma}\right)\right]}. \tag{1.4}$$

Stage Three: As discussed by Garrett (1983), the period of exponential growth will continue until the horizontal scale of the tracer patch exceeds that of the mesoscale eddies, which are typically order 50 km. Once this occurs, continued stirring by the eddies causes

12

tracer streaks to wrap around themselves, eventually making the patch more homogeneous. Subsequently, say for times long compared to the Lagrangian integral time scale, I_L, (see section 1.3.2 for definition), the rate of tracer dispersal may again be approximated as a diffusive process, with area

$$A_e = 8\pi\kappa_e t, \tag{1.5}$$

where $\kappa_e = \overline{\langle u'^2\rangle} I_L$ is an effective eddy diffusivity, and $\overline{\langle u'^2\rangle}$ denotes the mean squared eddy velocity.[1] The predicted concentration is then given by

$$C_e = \frac{M}{8\pi\kappa_e t}. \tag{1.6}$$

Using an effective eddy diffusivity $\kappa_e \approx 10^3$ m^{2}s^{-1} as characteristic of the open ocean, Garrett (1983) further predicted that the time it takes for tracer to reach this third stage is order one year, at which time the tracer patch will have a horizontal scale of approximately 360 km.

1.3 Statistics of Particle Dispersal

To further facilitate the discussion in the next two chapters, theoretical predictions for the intimately related problem of Lagrangian particle dispersal are reviewed. Again an idealized ocean is assumed which is horizontally homogeneous and statistically stationary over the scales of interest. This ocean has now been seeded with a large number of Lagrangian particles or neutrally buoyant floats. In the present section, a number of statistical quantities are defined that are used in later chapters to characterize the subsequent dispersal of such particles.

1.3.1 Mean and Eddy Displacements

Trajectories traced out by an individual Lagrangian particle are denoted by $x_{j_i}(t_k)$, where j identifies the particle, $i = (1,2)$ indicates (zonal, meridional) components, and t_k is the discretized time since launch. The Lagrangian velocities of individual particles are defined by $u_{j_i}(t_k) = \frac{d}{dt}x_{j_i}(t_k)$, where, in practice, a finite differencing scheme is used to

---

[1]I have assumed here that the eddy motion is isotropic, however, the result is readily generalized to the anisotropic case.

approximate $\frac{d}{dt}$. Ensemble averages of position and velocity as a function of time since launch are defined as

$$x_i(t_k) = \langle x_{j_i}(t_k) \rangle = \frac{1}{N(t_k)} \sum_{j=1}^{N(t_k)} x_{j_i}(t_k), \qquad (1.7)$$

$$u_i(t_k) = \langle u_{j_i}(t_k) \rangle = \frac{1}{N(t_k)} \sum_{j=1}^{N(t_k)} u_{j_i}(t_k), \qquad (1.8)$$

where the number of floats, $N(t_k)$, is allowed to vary in time in order to accommodate the real problem of float failure. Combined time and ensemble averaged velocity components, $\overline{\langle u_i \rangle}$, may also be defined such that

$$\overline{\langle u_i \rangle} = \frac{1}{M} \sum_{j,k} u_{i_j}(t_k), \qquad (1.9)$$

where M is the total number of observations. Eddy displacement and velocity are then defined by subtracting out the effects of the mean flow, *i.e.*,

$$x_i'(t_k) = x_i(t_k) - \overline{\langle u_i \rangle} \, t_k, \qquad (1.10)$$

$$u_i'(t_k) = u_i(t_k) - \overline{\langle u_i \rangle}. \qquad (1.11)$$

1.3.2 Spatial and Lagrangian Auto-Correlation Functions

Given an ensemble of Lagrangian particles, a useful characterization of the dominant length and time scales of the flow is provided by the spatial correlation functions (SCF) and Lagrangian auto-correlation functions (LACF), respectively. In chapter two, these spatial and temporal correlation functions are used along with the eddy kinetic energy to characterize the basic scales of the flow in the NATRE observations. These statistics are then applied to model results in order to calibrate the numerical model against the observations.

The isotropic SCF, $S_{ii}(\xi)$, are defined as

$$S_{ii}(\xi) = \frac{\langle v_i'(d) v_i'(d+\xi) \rangle}{\langle v_i'^2 \rangle}, \qquad (1.12)$$

where ξ is the separation distance from an arbitrary position, d, and v_i ($i = 1, 2$) represent the (transverse, longitudinal) components of velocity (hence the double subscripts $ii =$

14

(11, 22) denote (transverse, longitudinal) spatial correlation functions). The LACF, $R_{ii}(\tau)$, are defined as

$$R_{ii}(\tau) = \frac{\langle u_i'(t)u_i'(t+\tau)\rangle}{\overline{\langle u_i'^2\rangle}}, \qquad (1.13)$$

where τ is the time lag from an arbitrary time, t, and u_i ($i = 1, 2$) represent zonal and meridional components of velocity (the double subscripts $ii = (11, 22)$ denote (zonal, meridional) auto-correlation functions). The characteristic length scale of the flow is typically assumed to be given by the transverse SCF, and is generally taken to be equal to the separation distance of the first zero crossing of S_{ii}. The integral time scale, I_{ii}, is similarly assumed to be given by the corresponding LACF, and is typically assumed to be roughly half the value of the time lag of the first zero crossing. The (possibly anisotropic) integral time scale can be more rigorously defined in terms of the LACF as

$$I_{ii} = \int_0^\infty R_{ii}(\tau)d\tau, \qquad (1.14)$$

provided this integral converges (for isotropic turbulence, $I_{11} = I_{22} = I_L$).

1.3.3 Dispersion and Effective Eddy Diffusivity

Taylor (1921) showed how to estimate large scale stirring from Lagrangian observations. If the motion is statistically stationary and homogeneous, then the mean squared eddy displacement, i.e., the dispersion, is related to the mean squared eddy velocity, i.e., twice the eddy kinetic energy, through the relation

$$\langle x_i'^2(t)\rangle = 2\overline{\langle u_i'^2\rangle} \int_0^t \int_0^T R_{ii}(\tau)d\tau dT, \qquad (1.15)$$

where $R_{ii}(\tau)$ is the Lagrangian auto-correlation function defined above. (In what follows, the mean eddy kinetic energy (EKE) is defined as $\frac{1}{2}\overline{\langle u_i'^2\rangle}$.) For small τ, the auto-correlation function, R_{ii}, does not differ appreciably from unity, so equation (1.15) simplifies to

$$\langle x_i'^2(t)\rangle = \overline{\langle u_i'^2\rangle}\, t^2, \qquad (1.16)$$

or, equivalently,

$$\sqrt{\langle x_i'^2(t)\rangle} = \sqrt{\overline{\langle u_i'^2\rangle}}\, t. \qquad (1.17)$$

This says that for small times the dispersion is proportional to the time since release squared and the eddy kinetic energy (eq. 1.16), or equivalently, the standard deviation of particle displacement is proportional to the time since release and the rms eddy velocity (eq. 1.17).

15

For long times, R_{ii} should approach zero in a turbulent flow, so the first integral in equation (1.15) becomes saturated, *i.e.*,

$$\int_0^T R_{ii}(\tau)d\tau = I_{ii} = const. \tag{1.18}$$

In this case, equation (1.15) reduces to

$$\langle x_i'^2(t) \rangle = 2\overline{\langle u_i'^2 \rangle} I_{ii} t. \tag{1.19}$$

or, equivalently,

$$\sqrt{\langle x_i'^2(t) \rangle} = \sqrt{2\overline{\langle u_i'^2 \rangle} I_{ii} t}, \tag{1.20}$$

For long times, this says that the standard deviation of particle displacement is proportional to the square root of time. Equation 1.19 implies that for long times, particles disperse at a constant rate which is proportional to the mean squared eddy velocity and the integral time scale of the turbulence, *i.e.*,

$$\frac{d}{dt}\langle x_i'^2(t) \rangle = 2\overline{\langle u_i'^2 \rangle} I_{ii} = 2\kappa_{e_{ii}}. \tag{1.21}$$

This constant rate of dispersion, $\kappa_{e_{ii}}$, defines the large-scale effective eddy diffusivity of the turbulent flow. For isotropic turbulence, this should be the κ_e of equations (1.6) and (1.5).

Chapter 2

Results from the North Atlantic Tracer Release Experiment

This chapter provides a brief overview of the NATRE field observations. The observed horizontal distributions of passive tracer and Lagrangian particles are examined, and the statistics of the previous chapter used to quantitatively compare the observations to theoretical predictions.

2.1   Overview of NATRE

The NATRE field experiment was performed at a location 1,200 km west of the Canary Islands (see Ledwell *et al.*, 1993) in a region which is considered characteristic of open ocean conditions. The passive tracer component of the experiment, led by Dr. James Ledwell and Dr. Andrew Watson, involved the controlled release of a passive tracer (sulfur hexaflouride, SF_6) on a target density surface within the main pycnocline. The tracer concentration was observed over a series of sampling cruises with the primary objectives of estimating the diapycnal diffusivity across the main pycnocline, and studying lateral mixing and stirring on scales from 10 km to 1000 km in the open ocean. The latter is the focus of the present study. In conjunction with the tracer release, ten neutrally buoyant Sound Fixing and Ranging (SOFAR) floats were also deployed under the supervision of Dr. James Price and Dr. Phil Richardson (Price *et al.*, in preparation). The floats were pre-programmed to

spend the majority of their time at nearly the same depth as the tracer, and were tracked for up to one year following their deployment (May, 1992 - May, 1993), thus allowing a simultaneous view of passive tracer and Lagrangian particle dynamics.

2.2 NATRE Tracer

The tracer injection, performed between May 5-13, 1992, consisted of a series of closely spaced streaks in an area approximately $25 - 30$ km in horizontal extent. The target surface had a potential density of $\sigma_{.3} = 28.05$, which in this region of the ocean is at approximately 310 m depth. Sampling commenced immediately after the tracer was released, and consisted of a series of five cruises spanning a period of two and one half years. Specifically, sampling was performed during the two weeks after release (between 14-31 May 1992), five to six months later (October to November, 1992), one year after release (April to May, 1993), and two and one half years after release (November, 1995). The horizontal distribution of tracer (expressed as the depth integrated concentration) observed during the first year of sampling is shown in Figures 2.1, and 2.2.

The series of "snap-shots" as measured by the NATRE sampling cruises provides a vivid image of the effects of dispersion and diffusion in the open ocean. Of notable interest is the streak-like character of the tracer distribution observed during the October and November, 1992 surveys (Figure 2.1), presumably associated with exponential growth of tracer area as described in section 1.2.1. For this phase of the tracer dispersal, there appear to be two significant length scales which characterize the tracer distribution. One is the dominant length scale of the mesoscale eddies, which sets the radius of curvature of the streaks, and the second is the rms width of the streaks, which might be set by a balance between the effective small-scale diffusion (on scales less than the streak width) and the tendency of the mesoscale eddies to strain the tracer into streaks. Following Ledwell *et al.*, (1993), the theory of section 1.2.1 may be applied to estimate the rms strain rate, γ, and the small-scale diffusivity, κ_s, based on the observed tracer distribution. Assuming that the entire tracer patch was distributed in streaks similar to those observed, the predicted exponential growth of streaks, $L = L_s e^{\alpha \gamma t}$, with $\alpha = 1$, implies an rms strain rate of $\gamma \approx 3 \times 10^{-7}$ s^{-1}. Given the observed rms cross-streak width of $\sigma_s \approx 3$ km, a balance between along-streak strain and cross-streak diffusivity (*i.e.*, $\sigma_s = \sqrt{\kappa_s \gamma}$) then implies small-scale lateral diffusivity of $\kappa_s \approx 3$ m^{2}s^{-1} acting on scales less than about 10 km. This

18
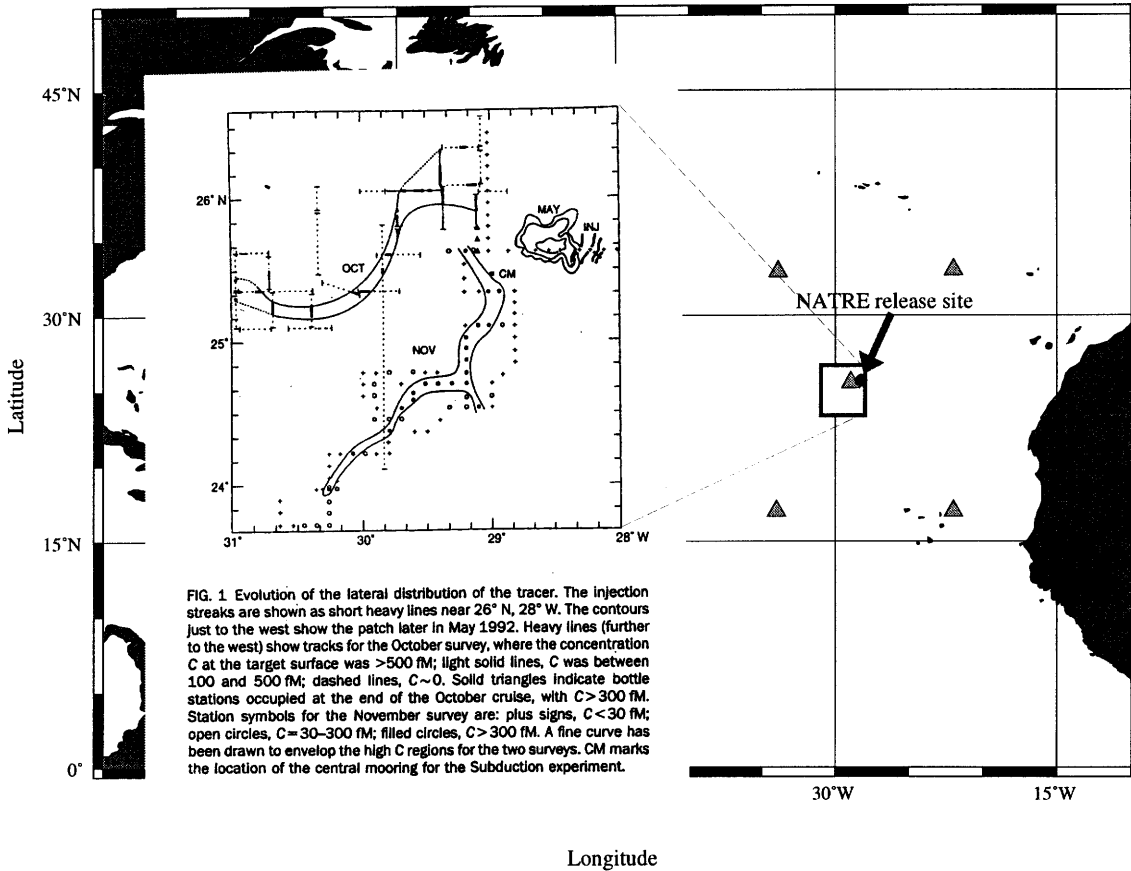
FIG. 1 Evolution of the lateral distribution of the tracer. The injection streaks are shown as short heavy lines near 26° N, 28° W. The contours just to the west show the patch later in May 1992. Heavy lines (further to the west) show tracks for the October survey, where the concentration C at the target surface was >500 fM; light solid lines, C was between 100 and 500 fM; dashed lines, C~0. Solid triangles indicate bottle stations occupied at the end of the October cruise, with C>300 fM. Station symbols for the November survey are: plus signs, C<30 fM; open circles, C=30–300 fM; filled circles, C>300 fM. A fine curve has been drawn to envelop the high C regions for the two surveys. CM marks the location of the central mooring for the Subduction experiment.

Longitude

Figure 2.1: Horizontal distribution of tracer, expressed as the depth integrated concentration, for the first six months of NATRE. The insert (taken from Ledwell et al., 1993) shows the location of the initial tracer injection streaks (marked INJ), contours of tracer two weeks after injection (marked MAY), and the two streaks observed in Fall, 1992 (marked OCT, NOV). Also shown are the locations of the five Subduction moorings (triangles).

19

Column Integral of Tracer - Spring, 1993
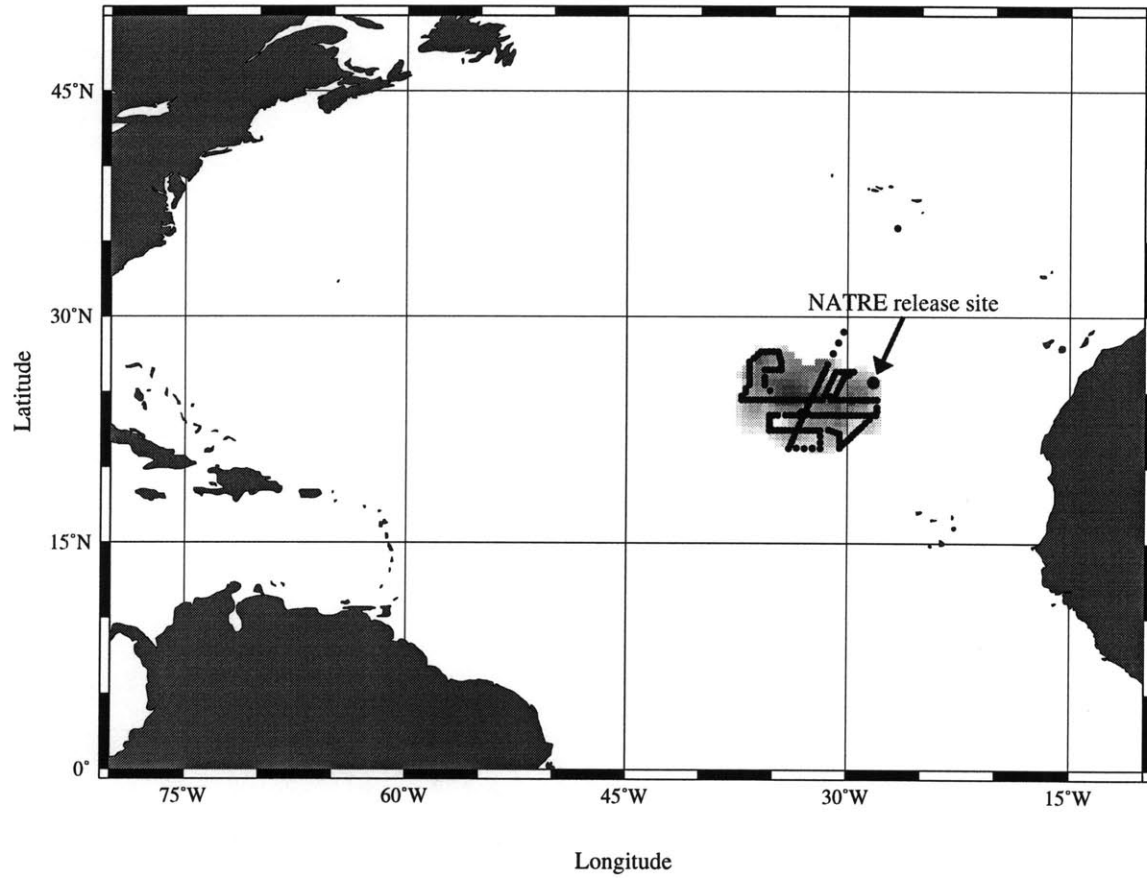
Figure 2.2: Horizontal distribution of tracer in May, 1993, showing a painted in tracer patch which is large compared to the mesoscale (Watson et al., 1993).

value of κ_s estimated by Ledwell et al., (1993) can be compared to the small-scale diffusivity estimated by Young et al. (1982) for shear dispersion by internal waves of $\kappa_s \approx 10^{-2}$ m^{2}s^{-1} which is presumed to act on scales of order 100 m. The two orders of magnitude discrepancy between these diffusivities suggests the presence of a highly efficient mixing process acting at scales of order 1–10 km (Ledwell, personal communication); this will be considered in further detail in chapters 3 and 4.

From the observed tracer distribution in May, 1993 and November, 1994, the size and direction of the mean flow was estimated based on the location of the center of mass of the tracer patch at different times. These mean Lagrangian velocities were compared to Eulerian means estimated from moored current meters from the Subduction experiment (the location of these moorings is shown in Figure 2.1) in order to assess the importance of strictly Lagrangian effects on tracer and float dispersion (e.g., such as might arise from a large-scale gradient in eddy diffusivity). Based on the estimated 99 $\pm$ 10% of the tracer found with the nearly two hundred stations of the May, 1993 survey (Watson et al., 1993), the mean flow characteristic of the first year was approximately $u = -1.0$ cm s^{-1}, $v = -0.2$ cm s^{-1} (Ledwell, personal communication). A similar calculation based on the estimated 50% of the tracer found over 41 stations of the November, 1994 survey, assuming the patch extended eastward about to the location of the injection site, gave approximately the same value of the mean flow (Ledwell, personal communication). These estimates are roughly in agreement with mean velocities computed from Subduction current meter data at about the same depth for the period following the NATRE tracer release (Brink et al., 1994). This agreement between Lagrangian and Eulerian estimates suggests that the movement of the center of mass of tracer was indeed due to a mean flow, and not some strictly Lagrangian effects (e.g., such as might arise from a large-scale gradient in eddy diffusivity).

From the May, 1993 and November, 1994 tracer distributions, an estimate was made of the large-scale effective eddy diffusivity, κ_e, using the relation $2\kappa_e = \frac{\partial}{\partial t}\sigma^2$ where σ^2 is the tracer variance (e.g., Fisher et al. 1979). This gave an effective eddy diffusivity of approximately 1×10^3 m^{2}s^{-1} (Ledwell, personal communication), which is consistent with estimates of particle dispersion based on the NATRE floats (see next section). Some degree of anisotropy was also evident in the tracer distribution, however, its magnitude has not yet formally been determined.

At this point, the theoretical predictions of section 1.2.1 may be compared to the NATRE observations. For simplicity, it is assumed that for long times, the tracer dispersal was isotropic with characteristic large-scale eddy diffusivity $\kappa_e = 1 \times 10^3$ m^{2}s^{-1} (see above).
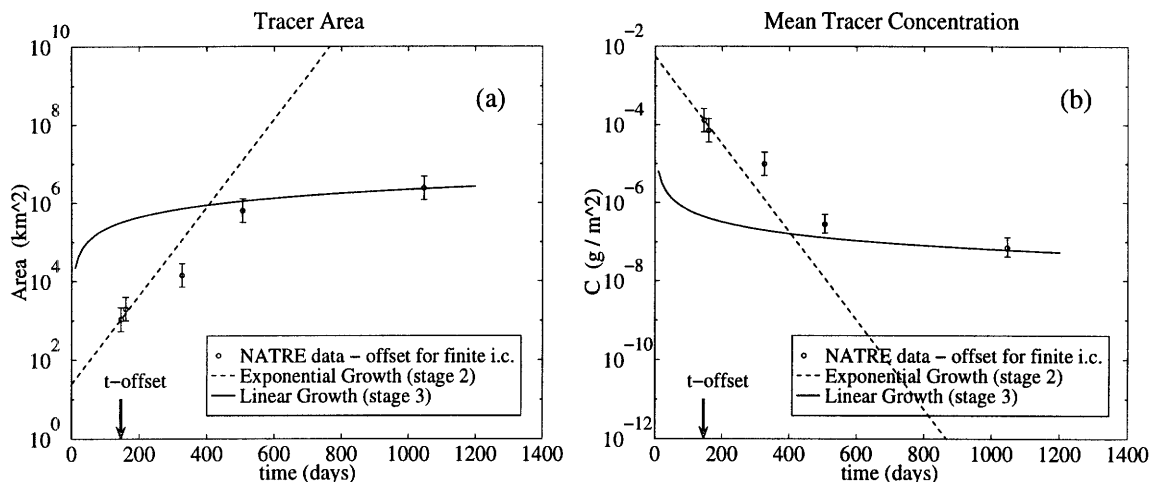
Figure 2.3: Exponential (dashed lines) and linear (solid lines) growth phases (stages 2 and 3 of section 1.2) of a) tracer area and b) mean concentration for a theoretical point release of passive tracer in a turbulent flow and for the five sampling periods of NATRE (open circles). Theoretical curves are for $\kappa_e = 1 \times 10^3$ m^{2}s^{-1}, $\kappa_s = 3$ m^{2}s^{-1}, $\gamma = 3 \times 10^{-7}$ s^{-1}, and $\alpha = 1$. Data points from NATRE are plotted with a time offset of approximately 150 days to compensate for the finite size of the initial release. Error bars correspond to a factor of 2 uncertainty in the area estimates.

Other parameters are a small-scale diffusivity, $\kappa_s = 3$ m^{2}s^{-1}, an rms strain rate, $\gamma = 3 \times 10^{-7}$ s^{-1} (consistent with Ledwell et al., 1993), and a coefficient for the exponential growth phase, $\alpha = 1$ (see equations (1.3) – (1.6)). The corresponding theoretical curves for tracer area and concentration are shown in Figure 2.3. For the NATRE data, area was estimated by eye from the insert in figure 2.1, taken from Ledwell et al. (1993), and from maps of the tracer distribution in cruise reports by Watson et al. (1993) and Ledwell et al. (1994). The mean concentration was computed simply as the total tracer released divided by the total area of the patch. Since the theoretical results are for the dispersal of a point release of passive tracer, and the initial tracer distribution in NATRE was of finite area, the NATRE data points are plotted with a time offset. (The time offset is the time it would take for the area of tracer from a point release to equal that of the NATRE tracer release.) From my estimate, the NATRE initial tracer distribution had an area of approximately 1075 km, corresponding to a time offset in Figure 2.3 of approximately 150 days. Comparing the data with the theoretical predictions, good agreement is found for the exponential-growth phase as well as for the linear regime at large times. This suggests that the effects of mesoscale stirring are indeed well described by Garrett's (1983) model, and

22

that for the NATRE experiment these effects can be parameterized using the above values of γ, κ_s, and κ_e.

2.3 NATRE Floats

Next, the NATRE float data is analyzed using the particle statistics of chapter 1. The overall goal of this is to characterize the kinematics of the mesoscale flow. The ten SOFAR floats released during NATRE were deployed along with the tracer in May, 1992, and were tracked for up to one year after deployment. Each float was pre-programmed to make daily excursions through a portion of the water column, while spending the majority of the day at a depth approximately equal to that of the target density surface. The floats were tracked acoustically, with fixes of their positions given twice per day by an array of moored listening stations. Zonal and meridional velocity components were computed from the float positions using a cubic spline interpolation method (Price *et al.*, in preparation). A more detailed description of the floats including their programming information is given in Appendix A.

For the purpose of computing ensemble statistics, the 10 NATRE floats provide a somewhat limited sampling of the Lagrangian flow. Therefore, the following analysis also incorporates data from four SOFAR floats of the Subduction Experiment (Price *et al.*, in preparation) which were deployed about 600 km north-east of the NATRE site in May, 1991. The Subduction floats were of the same type as those used in NATRE except that they were equipped to transmit data for two years after deployment. The four incorporated floats were advected south-westward through the site of the NATRE experiment slightly above the target density surface between May, 1991 and May, 1993 (see Appendix A).

Of the ten NATRE floats, three transmitted data for the full length of the experiment, four transmitted for between four and six months, and three failed a few days after deployment. Of the four Subduction floats, three transmitted data for two years, while one failed after the first year. In short, the ten NATRE floats provided a total of 57 float months, drifting in the region from $24^o - 34^o$ W and $21^o - 27^o$ N, while the four Subduction floats provide an additional 84 float months, drifting in the region from $23^o - 36^o$ W and $19^o - 30^o$ N. The life-span of each float is shown in Figure 2.4.
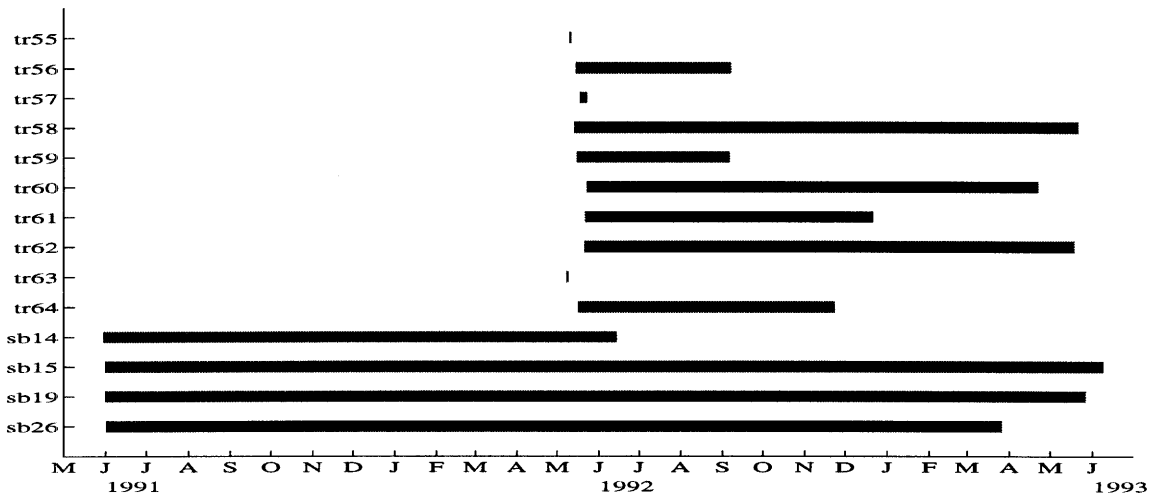
Figure 2.4: Float life-spans for NATRE (tr55-64) and selected Subduction floats (sb14,15,19,26).

2.3.1 Subjective assessment of eddy motions

As a first look at the float data, individual float trajectories may be examined in order to gain insight about the eddy characteristics of the NATRE region. Float trajectories are displayed in Figure 2.5. Loops in these trajectories are used to infer approximate sizes, strengths and propagation speeds of mesoscale flow features encountered by the floats. Figure 2.6 shows the full set of float trajectories with a subjective interpretation of eddy activity. The minimum criterion used for drawing an eddy along a particular float track was that the float made at least one complete loop while maintaining an approximately uniform azimuthal velocity. Loops which appeared to be part of a random walk were not accredited to an eddy. Table 2.1 lists each eddy from Figure 2.6 by number, along with the floats whose motions were accredited to it. Additional eddy information given in Table 2.1 is discussed below.

Eddy sizes were deduced on the assumption that a float which was briefly trapped and then released by an eddy must have remained on the perimeter of the eddy while it was trapped. The eddy size (diameter) was then estimated as the maximum displacement of the float normal to the apparent direction of eddy propagation. When the propagation direction was not discernible, eddy size was estimated as the average diameter of the loops. The average diameter of the eddies listed in table 2.1 is approximately 72 km. Inferred eddy paths indicated by bold arrows in Figure 2.6 suggest a general trend of south-westward eddy
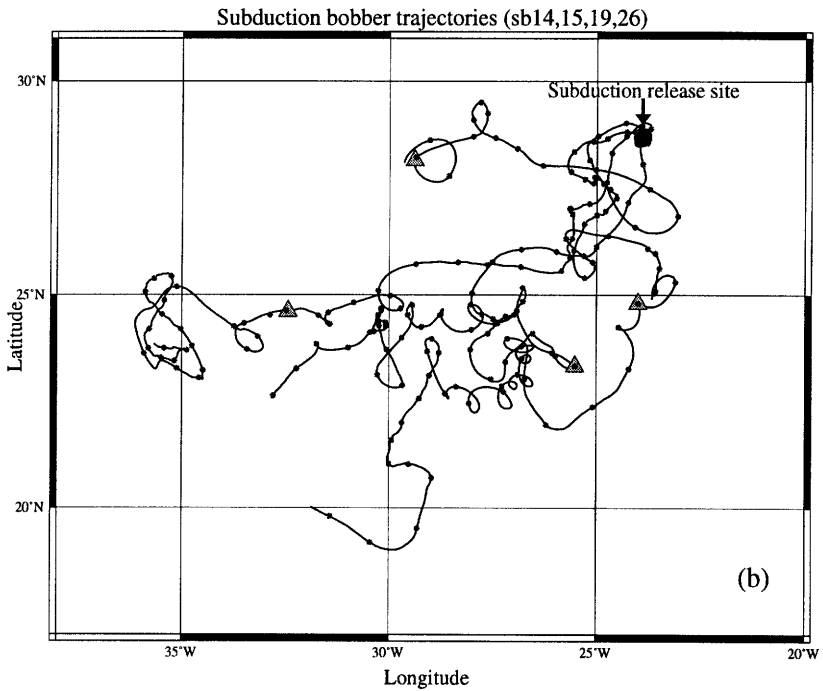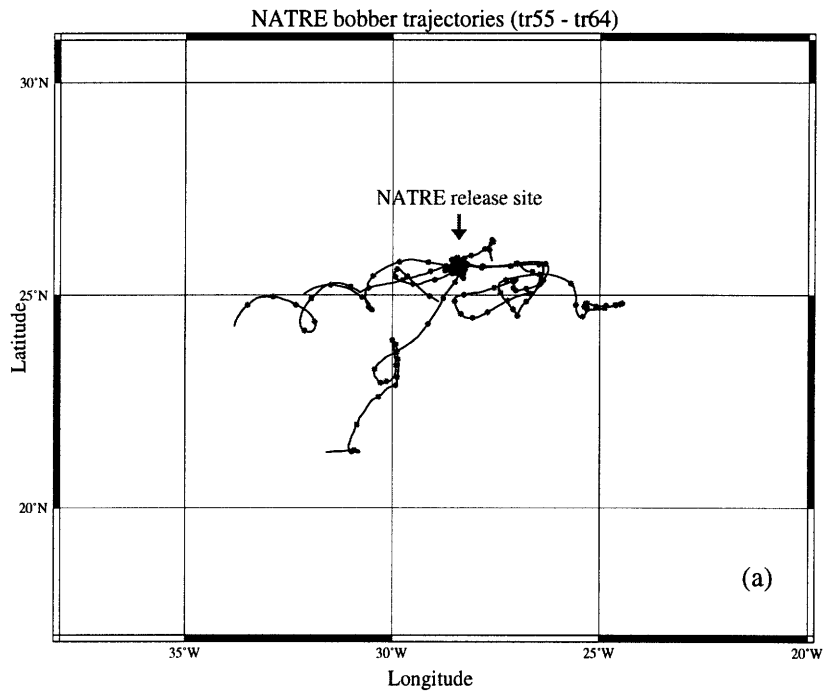
Figure 2.5: Float trajectories for a.) 1992-1993 NATRE floats (tr55-64), b.) 1991-1993 Subduction floats (sb14,15,19,26). The locations of the four Subduction floats at the time of the NATRE release are marked by triangles. Tick marks along trajectories correspond to 30 day intervals since release.
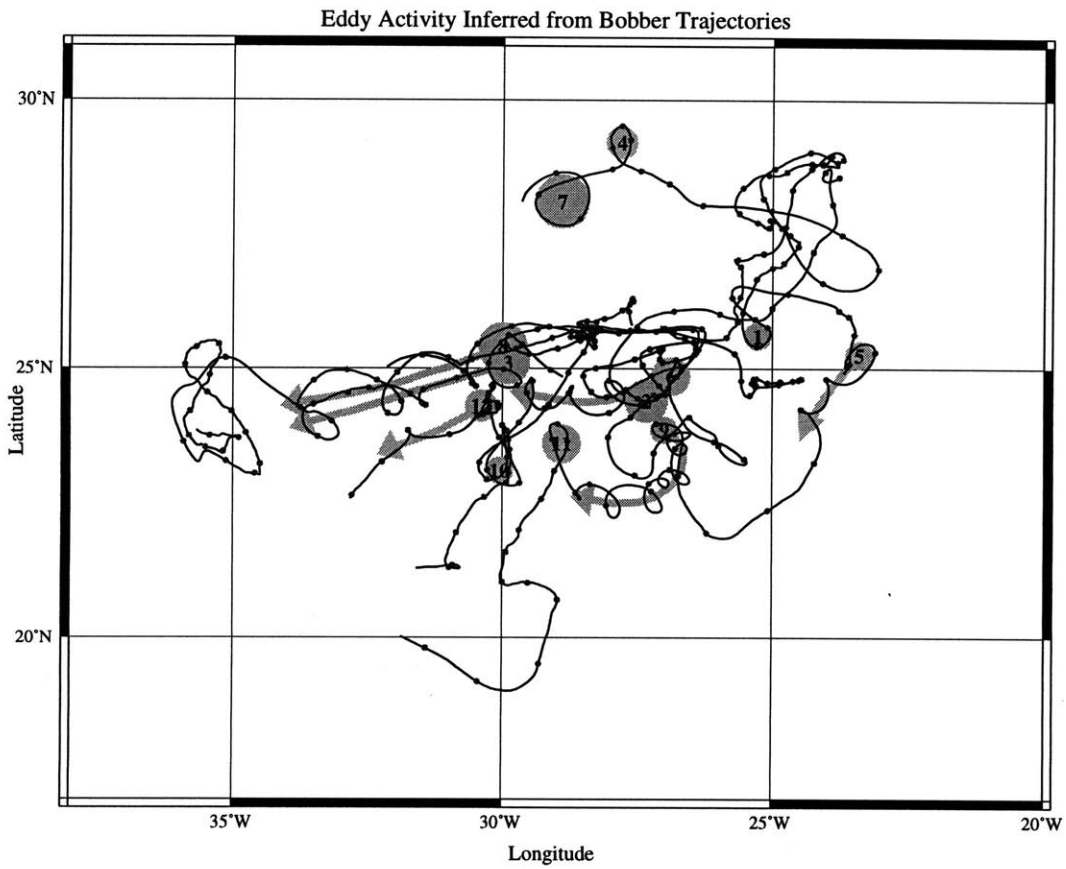
Figure 2.6: NATRE and Subduction float trajectories of Figure 2.5 with a subjective interpretation of eddy activity. Eddy numbers correspond to those listed in table 2.1.

Eddy	Float	Dates	$\lvert u_{trans}\rvert \frac{km}{day}$	Diam km	Loops	$\lvert u_{azim}\rvert \frac{cm}{sec}$	$\zeta \times 10^{-6} \frac{1}{sec}$
1	sb19	11/01/91-12/01/91	–	53	1	6.4	2.4
2	sb15	10/28/91-12/28/91	–	85	1	5.1	1.2
3	sb26	12/20/91-06/20/92	2.3	85	3	5.1	1.2
4	sb14	02/23/92-04/23/92	–	61	1	3.7	-1.2
5	sb19	03/01/92-05/01/92	2.8	53	2.5	8.0	-3.0
6	sb15	05/15/92-10/15/92	2.2	76	4	3.7	-1.0
7	sb14	04/23/92-06/19/92	–	105	1.3	8.9	1.7
8	tr56	06/01/92-09/07/92	2.7	95	1.2	4.3	0.9
8	tr64	08/05/92-11/23/92	2.9	95	1.3	4.2	0.9
9	sb19	07/01/92-11/01/92	2.8	53	7	11.2	4.2
10	tr58	11/01/92-01/01/93	–	53	1	3.2	1.2
10	sb15	11/01/92-12/01/92	–	53	1	6.4	2.4
11	sb19	11/15/92-12/30/92	–	76	1	6.2	-1.6
12	sb15	03/21/93-05/21/93	3.8	61	1.5	5.6	-1.8

Table 2.1: Subjective assessment of eddy activity gleaned from NATRE and selected Subduction floats.

translation. Where eddy paths were unambiguous, eddy translation speeds were calculated based on the total eddy displacement and the length of time that floats were trapped. These values, listed in table 2.1, yield an average translation speed of 2.8 km day^{-1}, or 3.2 cm s^{-1}, which is roughly twice the speed of the mean flow estimated from either the NATRE tracer (see section 2.2) or the full float data set (see next section). The enhanced translation speeds of the eddies relative to the mean flow may be due to the nonlinear interactions between the coherent vorticies and a zonal mean shear flow (a problem that has received some attention in the field of meteorology, e.g., Williams and Chan, 1994), however, the exact mechanism of such interactions is not fully understood, and is beyond the scope of the present study.

Azimuthal velocities on the eddy perimeters were estimated based on the time required for a float to complete a given number of loops. These were used to calculate the relative vorticity associated with each eddy. A roughly even distribution between cyclonic and anti-cyclonic eddies was found, with an average relative vorticity of $\overline{\zeta} = (2.0 \pm 1.1, -1.7 \pm 0.8) \times 10^{-6}$ s^{-1} (see table 2.1), or approximately $0.03f$, where f is the Coriolis frequency at $25°$ N.

Frequency spectra of the zonal and meridional float velocities were computed by breaking the data into 300, 200, and 100 day long segments. These are plotted in variance preserving form in Figure 2.7. Both velocity components show marked peaks at frequencies corresponding to about 15 days as well as lesser peaks corresponding to periods of 1 − 2
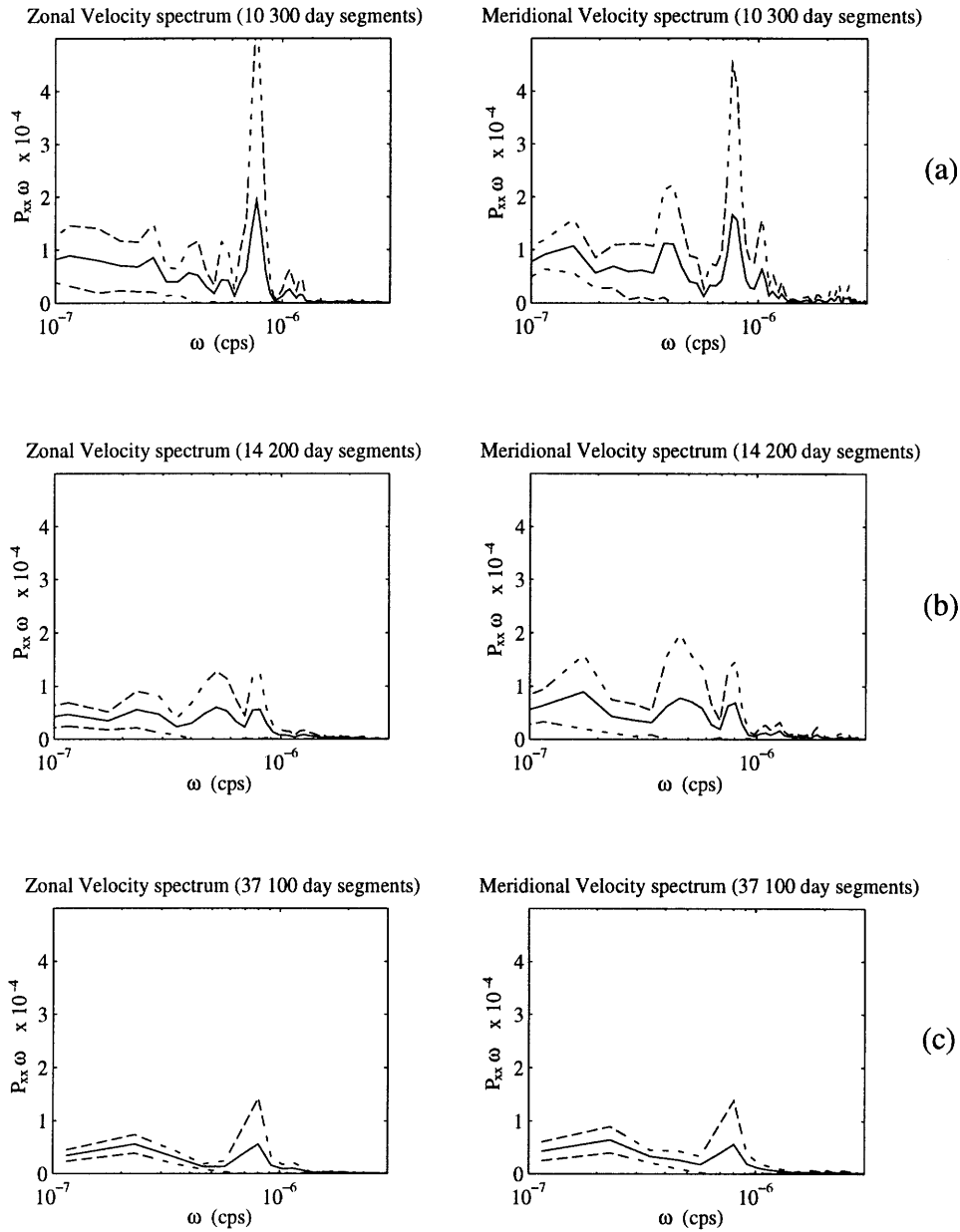
Figure 2.7: Frequency spectra of zonal and meridional float velocities computed using a) 300, b) 200, and c) 100 day long data segments, with the number of segments used in each case indicated on the plots. Solid lines represent the frequency spectra and dashed lines represent the uncertainty. Major peaks correspond to periods of about 2 weeks and 1–2 months.

months. Examination of frequency spectra for individual float records (not shown) suggests that the prominent peak at 15 days is due to the very energetic eddies numbered 5 and 9 in Figure 2.6, while the 1–2 month peaks are due primarily to eddies numbered 3, 6, 8, and 12.

2.3.2 Lagrangian Particle Statistics

Application of the Lagrangian particle statistics of section 1.3 to these data requires two basic assumptions. The first is that the flow field is statistically stationary, and the second is that it is horizontally homogeneous. Examination of current meter data from the central mooring of the Subduction experiment (Brink *et al.*, 1993) suggest that within the main pycnocline and for time scales greater than about 6 months the stationarity assumption is well grounded. As for horizontal homogeneity, one might question the validity of this assumption as the tracer and particle displacement become large. However, for the sake of simplicity, such effects as gyre scale horizontal shear and gradients in eddy diffusivity are ignored. Having made these assumptions, estimates are made of zonal and meridional mean velocities, eddy kinetic energies, dispersion, and diffusivities. Spatial and Lagrangian auto-correlation functions are also computed, and are used in chapter 3 in comparisons between observations and numerical simulations. As mentioned above, these statistics are computed for the combined data set consisting of the ten NATRE floats plus the four Subduction floats described above. (See Appendix A for a discussion of the statistics of the NATRE and Subduction floats separately.)

Mean Flow and Eddy Kinetic Energy

Time series of ensemble averaged velocity components are plotted in Figure 2.8. The mean transport velocities computed as in equation (1.9) are $(u, v) = (-1.2 \pm 0.3, -0.9 \pm 0.2)$ cm s^{-1}, while the zonal and meridional components of the combined time and ensemble-averaged EKE are $\frac{1}{2}\langle \overline{u'^2_{(1,2)}} \rangle = (8.1 \pm 1.0, 8.0 \pm 1.2)$ cm^2 s^{-2}. Errors are computed as the square root of the variance divided by the number of degrees of freedom where the number of number of degrees of freedom is computed as the record length divided by twice the
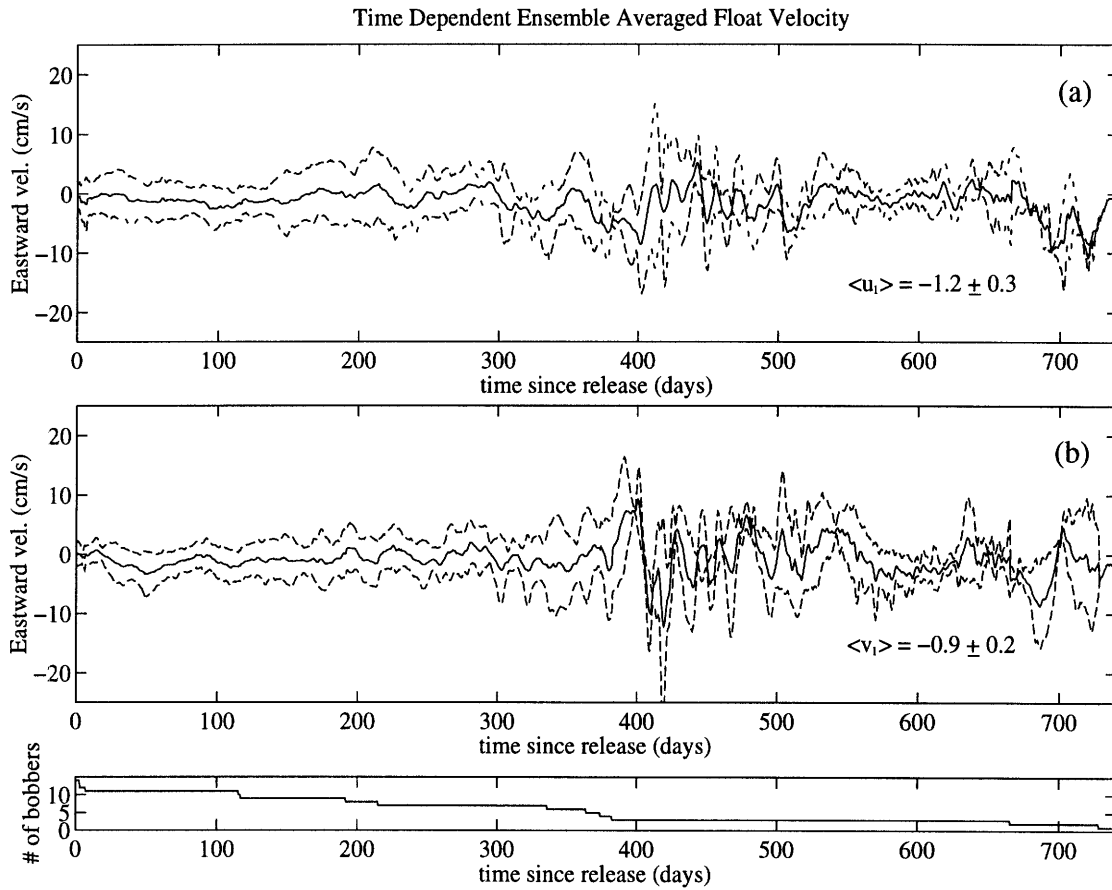
Figure 2.8: Time series of a) zonal (positive eastward) and b) meridional (positive northward) ensemble averaged velocity computed from NATRE and Subduction floats. Solid lines are the velocities and dashed lines indicate uncertainties (see text). The corresponding mean transport velocities are indicated in each figure. Also shown is the number of floats as a function of time that made up the ensemble averages.

30
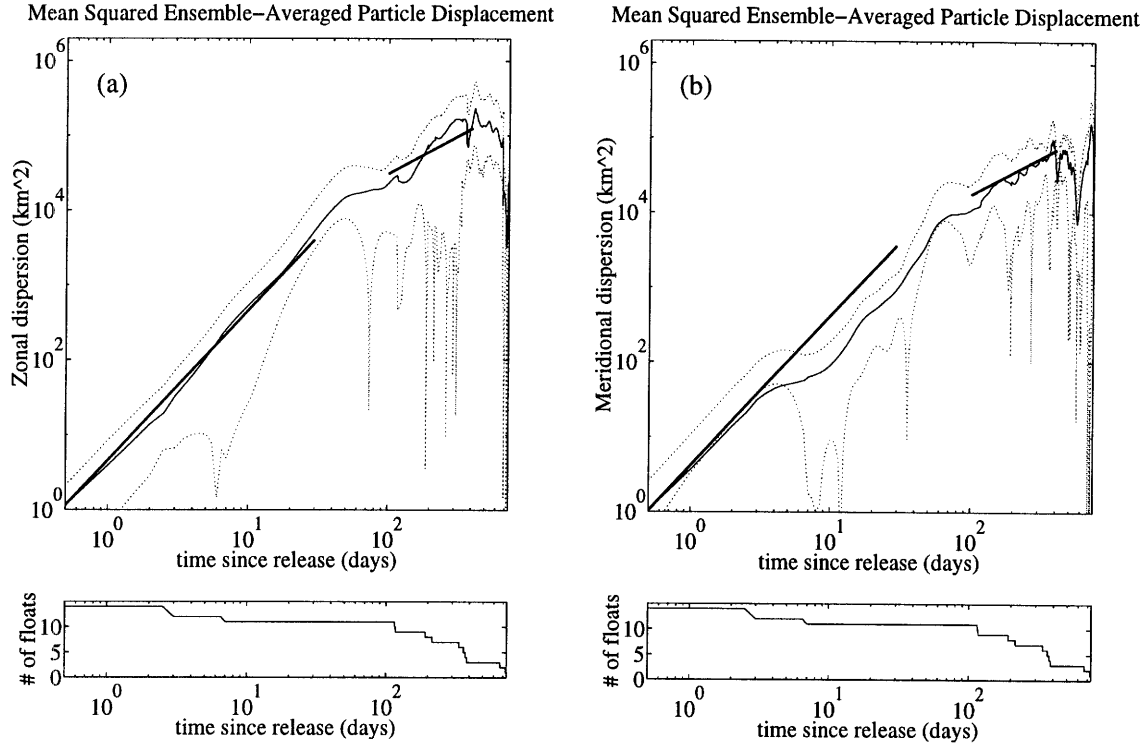
Figure 2.9: Time dependent a) zonal and b) meridional ensemble-averaged particle dispersion computed from NATRE and Subduction floats showing t^2 and t growth rates for short and long times, respectively. Solid lines are dispersion curves while dotted lines indicate the uncertainty. Bold solid lines have slopes of 2 and 1 on the log-log plot. Also shown are the number of floats as a function of time that made up the ensemble averages.

integral time scale ($(I_{11}, I_{22}) \approx (10.6, 5.4)$ days, see below).[1] The mean velocities computed from the float data are roughly in agreement with those estimated in section 2.2 from the tracer data, and thus consistent with the idea that Lagrangian particles and passive tracer are advected similarly.

Dispersion and Diffusivity

The ensemble averaged particle dispersion, $\langle x_i'^2(t) \rangle$, is plotted in Figure 2.9. For limiting cases of small and large t, the curves indicate the predicted t^2 and t growth rates,

---

[1]Ensemble means were computed under the assumption that each float represented an independent particle. This seems sensible for most of the data set, except for times shortly after release, when floats are likely to be within the same flow features and behave in a spatially coherent fashion. In this case, one must take care to account for the fewer degrees of freedom.

respectively. For small times, equation (1.16) implies that on a log-log plot of dispersion $vs.$ time the EKE should be given by the height of the dispersion curves ($i.e.$, it is proportional to the slope of these curves for small times). Figure 2.9 thus suggests EKE values of $\frac{1}{2}\overline{\langle u'_{(1,2)}{}^2\rangle} = (2.6 \pm 3.1, 2.4 \pm 4.7)$ cm^2 s^{-2}, where the uncertainty is computed as the square root of the variance divided by the number of independent pieces of data. These values of EKE are considerably lower than those made from the full record (above), most likely because of a bias at small t which results from the reduced number of degrees of freedom for small times (see earlier footnote). Since the previous direct estimates of EKE utilize the full data record, and hence limit this effect by incorporating a larger number of degrees of freedom, the previous estimates will be used to compute the eddy diffusivities in the next section.

For long times, equation (1.21) suggests that the diffusivities, $\kappa_{e_{ii}}$, are given by the slope of the dispersion curves (see Figure 2.9). A weighted linear least squares fit to the dispersion curves between $t = 100$ and $t = 400$ days, where the dispersion at time t is weighted by the variance of the mean, $\sigma_i^2/N(t)$, yields $\kappa_{e_{(11,22)}} = (6.0 \pm .17, 2.1 \pm .06) \times 10^3$ m^{2}s^{-1}. The uncertainty here is based on the goodness of the least squares fit, and thus should indicate how well this data set can be described by the classical diffusion formulation. These estimates of κ_e are approximately six times larger than those estimated from tracer distributions in Spring, 1993, and 2 to 4 times larger than those estimated in Fall, 1994. This discrepancy may be a result of the small number of independent float observations used in the calculation (it also seems that the small uncertainties here are likely fortuitous, given the small number of degrees of freedom). This is likely to be the case, since estimates of κ_e based on the product of the integral times scale and EKE (see next section) give closer agreement with κ_e estimates from tracer distributions.

Spatial and Lagrangian Auto-Correlation Functions

Having estimated the eddy kinetic energy and effective eddy diffusivity, the spatial and Lagrangian auto-correlation functions described in section 1.3.2 can be used to find the characteristic length and time scales of the mesoscale flow.

The transverse and longitudinal SCF's are plotted in Figure 2.10 along with the number of float pairs available for a given separation distance. Although the curves are somewhat noisy due to the limited number of floats, the expected tendency towards zero correlation for large separation distance is apparent. Based on the first zero crossing of
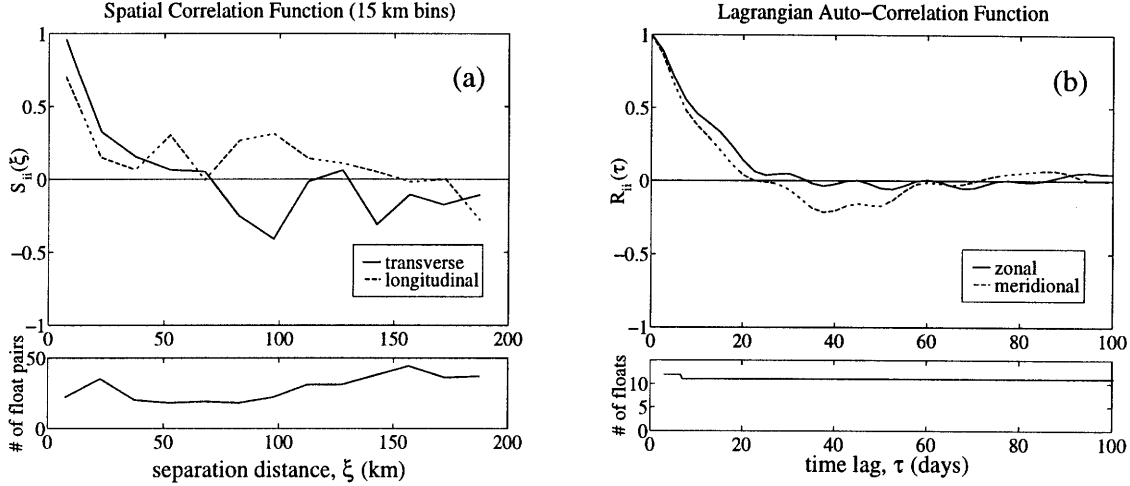
Figure 2.10: a.)Transverse (solid line) and longitudinal (dashed line) spatial correlation functions computed from NATRE and Subduction floats along with the number of float pairs used for a given separation distance. The covariances were averaged over 15 km bins of separation distance. b.) Zonal (solid line) and meridional (dashed line) ensemble-averaged Lagrangian auto-correlation functions computed from NATRE and Subduction floats along with the number of floats used for a given time lag.

the transverse correlation function the estimated length scale for the NATRE region is 70 km, which is (not surprisingly) roughly comparable to the estimated average eddy diameter from Table 2.1.

The zonal and meridional Lagrangian auto-correlation functions are plotted in Figure 2.10 along with the number of floats used for a given time lag. Comparing the zonal and meridional auto-correlation functions, a slight anisotropy is apparent, with the meridional auto-correlation function showing a small negative lobe after its first zero crossing. (The fact that this negative lobe, which is indicative of eddy or wave-like motions, shows up in only the meridional auto-correlation is consistent with theoretical expectations for planetary Rossby waves in the presence of a north/south vorticity gradient.) Figure 2.10 shows that the first zero crossings of the LACF occur between approximately 20 and 35 days, while it appears that the integrals of the LACF are probably saturated by τ equal to about 40 days for the zonal correlation function and 60–70 days for the meridional correlation function. The location of the change in slope of the dispersion curves in Figure 2.9 imply similar saturation times of approximately 50 days for the zonal correlation function and 60–70 days for the meridional correlation function. Integrating the LACF's using 100 days as the upper

limit of the integral of $R_{ii}(\tau)$, the integral time scales from equation (1.14) are

$$\begin{cases} I_{11} = 10.6 \quad \text{days} \\ I_{22} = 5.4 \quad \text{days} \end{cases} \tag{2.1}$$

for the zonal and meridional components, with 95% confidence limits of $(+5.4, -4.1)$, and $(+2.8, -2.8)$ days, respectively, estimated using the bootstrap method (Press *et al.*, 1986).

From these integral time scales and the combined time and ensemble-averaged EKE, equation (1.21) gives a second estimate of the zonal and meridional diffusivities,

$$\begin{cases} \kappa_{e_{11}} = 1.5 \ (+0.8, -0.6) \times 10^3 \ \text{m}^2\text{s}^{-1} \\ \kappa_{e_{22}} = 0.8 \ (+0.4, -0.4) \times 10^3 \ \text{m}^2\text{s}^{-1} \end{cases} \tag{2.2}$$

where error estimates are based on the uncertainties of EKE and I_{ii} computed above. These estimates of κ_e are in agreement with those computed from the tracer data in the previous section.

Chapter 3

Numerical Simulations of Passive Tracer and Lagrangian Particles

In the previous chapter, qualitative and quantitative agreement was found between observations from NATRE and simple theoretical predictions for tracer and particle dispersal in a homogeneous turbulent flow. In this chapter, a numerical model is used to determine the biases and uncertainties associated with the estimates of the rms strain rate, the small-scale diffusivity, and the effective eddy diffusivity made from the NATRE field observations. Within the scope of this objective also lies the question of whether the advection and diffusion of Lagrangian particles and passive tracer in the open ocean are well described and predicted (in a statistical sense) by the barotropic vorticity models which have traditionally been used to study this problem (e.g., Haidvogel and Keffer, 1982; Babiano et al., 1987; Holloway and Kristmannsson, 1984). The barotropic vorticity model used here is similar to the one used by Haidvogel and Keffer (1982), with the major difference being the form of the *ad hoc* forcing and dissipation terms used to achieve a statistically stationary homogeneous flow. The model is calibrated so that the statistics of the model floats agree as closely as possible with those computed for NATRE in the previous chapter. The model tracer field is then examined in detail and compared with both observations and theoretical predictions.

In this chapter, the model and its governing equations are introduced. Three specific criteria are used to calibrate the model with the observations. A typical model run, selected from an ensemble of runs which meet these criteria, is described in order to compare the

statistics of model floats to statistics from the NATRE observations Finally, the computed model tracer fields are examined in detail in order to assess qualitative as well as quantitative agreement with both the NATRE tracer data and the theoretical predictions made in chapter 1.

3.1 The Barotropic Vorticity Model

The numerical model is a semi-spectral, vorticity model (originally by Dr. William Dewar, and later modified by Dr. Glenn Flierl) which was run for a barotropic layer of constant depth and with a mean vorticity gradient in the y-coordinate direction. This model was chosen based on two criteria: it can simulate the advection and diffusion of a passive tracer efficiently and with considerable resolution and numerical accuracy; and it is simple, yet still capable of emulating the statistics of the flow in the open ocean in terms of EKE and characteristic length and time scales. This configuration is intended to be an idealization of a single isopycnal layer in the ocean. The omission of baroclinicity is not meant to suggest that it is unimportant in the ocean, but rather that the flow kinematics relevant to this study may be reproduced well enough in a barotropic model (the limits of this assumption are discussed in Appendix B). A detailed description of the numerical model is given in Appendix C.

3.1.1 Governing Equations

The model solves the vorticity equation for a single barotropic layer,

$$\frac{D}{Dt}q = \frac{\partial q}{\partial t} + J(\psi, q) = \kappa_s \nabla^2 q + D + F, \tag{3.1}$$

where q is the absolute vorticity, given by

$$q = \nabla^2 \psi + f_o + \beta y, \tag{3.2}$$

ψ is the stream function, which satisfies

$$(u, v) = \hat{k} \times \nabla \psi = \left(-\frac{\partial \psi}{\partial y}, \frac{\partial \psi}{\partial x} \right), \tag{3.3}$$

$f_o + \beta$ is the planetary vorticity, κ_s is the explicit small-scale viscosity, and D and F are *ad hoc* dissipation and forcing terms which are not attributed to physical processes (these will

36

be discussed in the next section). Using the stream function computed from equation (3.1), the evolution of a passive tracer field is computed from the advective-diffusive equation

$$\frac{D}{Dt}\theta = \frac{\partial \theta}{\partial t} + J(\psi, \theta) = \kappa_s \nabla^2 \theta, \tag{3.4}$$

where the explicit small scale diffusivity, κ_s is taken to be the same as in equation (3.1). The motion of Lagrangian particles in the model is computed using only the left hand side of equation (3.4).

The model is run on a $2\pi \times 2\pi$ square domain, with doubly periodic boundaries, and 128 grid points in each direction. To avoid ambiguity when comparing model results to observations, model results are given in non-dimensional form, while dimensional units are used when speaking of observations. In order to make model parameters such as EKE and planetary β correspond to realistic values for the NATRE experiment, the following velocity, time, and space scales are chose for redimensionalization,[1]

$$U = 4 \text{ cm s}^{-1} \tag{3.5}$$

$$T = 2.5 \times 10^6 \text{ s} \approx 29 \text{ days} \tag{3.6}$$

$$L = 100 \text{ km.} \tag{3.7}$$

i.e., the correspondence between non-dimensional model units and dimensional units is given by

$$[x, y, t, u, v] = [Lx^*, Ly^*, Tt^*, Uu^*, Uv^*], \tag{3.8}$$

where the dimensional variables are on the left hand side and the non-dimensional variables are starred quantities on the right hand side.

3.1.2 Calibration with NATRE Float Statistics

The model forcing and dissipation parameters were chosen so that the resulting flow field was similar in a statistical sense to that of the NATRE region. Three quantities are used to determine this: the eddy kinetic energy, a characteristic length scale determined by the spatial correlation function, and the Lagrangian integral time scale.

---

[1]Note that the non-linear system is characterized by an advective time scale, $T \sim L/U$, so that once U is chosen by means of the EKE, L and T are no longer independent

Statistical Stationarity and Homogeneity – Model Forcing and Dissipation

In order to apply the statistical methods of chapter 1, it is necessary that the model achieve a statistical equilibrium in which the flow is approximately stationary in time and homogeneous in space. However, if this model were left unforced, the inverse energy cascade of 2-D turbulence would soon lead to excessive energy at the gravest wavenumber (*e.g.*, Rhines, 1975). Thus for "spin-down" calculations, even if numerical diffusion is small, the flow soon evolves to scales which are too large to be considered homogeneous turbulence (the flow becomes dominated by a single, basin-scale dipole). If the planetary vorticity gradient, β, is sufficiently large (*i.e.*, the β "arrest scale", $\sqrt{U/\beta}$, is small compared to the characteristic length scale), the inverse cascade may be interrupted by the formation of zonal jets (*e.g.*, Rhines, 1975). However, in achieving a homogeneous turbulent flow as a stationary state, this is scarcely an improvement.

In order to circumvent the 2-D cascade, a rather *ad hoc* means was used to gain control of the distribution of energy over different scales in the model. Specifically, damping and forcing terms, D and F, were included in the governing equation (3.1) to remove energy that "piles up" at large scales and to inject energy at slightly smaller scales. The dissipation term is a scale-selective "friction" of the form

$$D = \mu_L \nabla^{-2} q, \qquad (3.9)$$

where the "large-scale viscosity", μ_L, has units $\mathrm{m^{-2} s^{-1}}$ (*e.g.*, Babiano *et al.*, 1987). (This "large-scale" dissipation is simply a high-pass filter.) To compensate for the overall energy loss due to this large-scale dissipation, a scale-selective forcing was imposed which puts energy in over a specified wavenumber band (typically a narrow band at low wavenumbers). For this forcing function, a random Markovian formulation is used, *i.e.*,

$$F_n \equiv \hat{F}(1 - R^2)^{\frac{1}{2}} e^{i\phi} + R F_{n-1}, \qquad (3.10)$$

where $\hat{F}$ is the wavenumber dependent forcing amplitude, ϕ is a random phase in $[0, 2\pi]$, R represents a forcing time scale ($R \equiv [1 - \frac{1}{2}\delta]/[1 + \frac{1}{2}\delta]$, where $\delta = \Delta t / \tau_f$, Δt is the numerical time step and τ_f is the forcing correlation time), and the subscript on F denotes the timestep (*e.g.*, Maltrud and Vallis, 1991). In order to avoid imposing an external time scale on the flow, τ_f was chosen to be no more than ten times the numerical time step so that the forcing was nearly random in time. By adjusting these forcing and dissipation terms, the shape of the energy spectrum in the model was controlled, and thus the desired stationarity and homogeneity achieved.

Eddy Kinetic Energy

Given a statistically stationary, homogeneous, turbulent flow, model calibration first required that the EKE computed from an ensemble of model floats agree with the EKE computed from the NATRE floats. To satisfy this, the scale and amplitude of the forcing, F, and the large-scale dissipation, D, were set in the model, and the model was "spun-up" for approximately 12 non-dimensional time units, or about 1 year. Thirty seven model floats were then simultaneously released at the center of the model domain in a closely spaced array of diameter approximately 0.4 non-dimensional units, or 40 km. Integration was continued for an additional 12 non-dimensional time units, and the ensemble EKE was computed from the model floats in the same way as for the NATRE floats in chapter 2.

Spatial and Lagrangian Auto-Correlation Functions

The second and third criteria for a "well calibrated" model are that the characteristic model length and time scales estimated from the isotropic SCF and zonal and meridional LACF are approximately the same as those computed from the NATRE floats. In practical terms, having specified the EKE in the model as described in the previous section, length and time scales in the model were adjusted simultaneously. As a first step in achieving the desired length scales, the model forcing was set to inject energy over a narrow wave number band, $3 < K < 4$, where $K = \sqrt{k^2 + l^2}$ is the total wavenumber. This corresponds to dimensional wavelengths between 160-210 km, *i.e.*, roughly the same as the typical eddy scale observed in NATRE. Next, the amplitudes of both the forcing and dissipation were simultaneously adjusted in order to achieve the desired degree of anisotropy in the LACF, while still maintaining the desired energy level in the model. In other words, the amplitudes of the isotropic forcing and dissipation terms were adjusted to partially offset the anisotropic tendencies of the planetary beta term. That the space and time scales as well as the anisotropy are not explicit parameters which can be set in the model *ab initio*, but rather had to be diagnosed from the steady solution made this calibration a laborious task. This task was further complicated by the fact that a barotropic model is being forced here to simulate a flow which is undoubtedly some combination of barotropic and baroclinic dynamics. As a result, there are inherent limitations on how well the model

Parameter	Symbol	Nondimensional value	Dimensional value
grid spacing	Δx	.049	4.9 km
time step	Δt	.003	2.08 hours
spin-up time		12.62	1.0 year
run time		12.62	1.0 year
planetary vorticity gradient	β	5.19	$2.07 \times 10^{-8}\ \mathrm{km}^{-1}\mathrm{s}^{-1}$
lateral dissipation	κ_s	2.5×10^{-3}	$10\ \mathrm{m}^2\mathrm{s}^{-1}$
large-scale dissipation	μ_L	1	$4.0 \times 10^{-17}\ \mathrm{m}^{-2}\mathrm{s}^{-1}$
mean forcing amplitude	$\hat{F}$	4.8×10^4	$7.7 \times 10^{-9}\ \mathrm{s}^{-2}$
forcing wavenumber band		$3 < K < 4$	$\frac{2\pi}{209.4} < K < \frac{2\pi}{157.1}\ \mathrm{km}^{-1}$
forcing time scale	τ_f	.0215	15.0 hours

Table 3.1: Model parameter settings used in the model run described in the text. Non-dimensional model units are scaled to dimensional physical units via $L = 100$ km, $T = 2.5 \times 10^6$ s, and $U = 4\ \mathrm{cm}^{-1}\mathrm{s}^{-1}$.

is able to reproduce the statistics of the observations (see Appendix B for a more detailed discussion of model limitations).

3.2 Spin-up of a Typical Model Run

Model parameter settings for a typical model run which meets the calibration criteria outlined in the previous section are listed in Table 3.1 along with their dimensional counterparts, where appropriate. The typical model run described here is one of 10 realizations examined, each of which used the parameter values of Table 3.1, but a different random phase forcing. In the interest of brevity, one run was subjectively chosen as representative of the ensemble, and will be presented here.

The model was spun-up from an initial condition in which the stream function was assigned a random phase and an amplitude such that its energy spectrum was similar to the expected equilibrium spectrum. This was done in order to reduce the amount of time needed for the flow to reach statistical stationarity. For a typical run, spin-up time was approximately 12 non-dimensional time units, or about one year. Figure 3.1 shows the domain-averaged Eulerian kinetic energy and the evolution of the energy spectrum for the spin-up of the typical model run. By visual inspection of energy spectra, it appears that the model reaches approximate stationarity within a few non-dimensional time units, although due to the random nature of the model forcing, fluctuations of the domain averaged kinetic energy still occur.
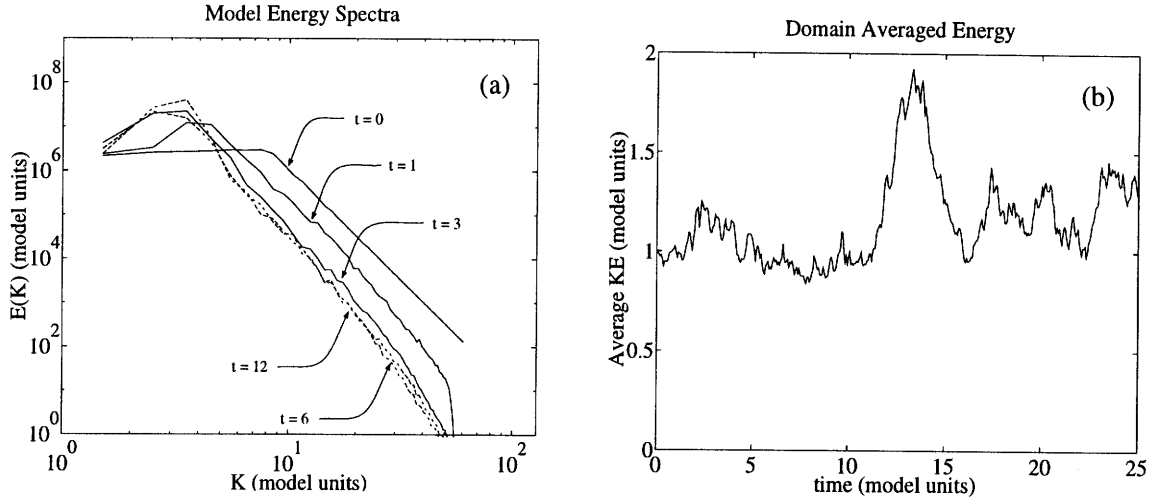
Figure 3.1: a) Model energy spectra during spin-up of a typical model run showing the evolution to a statistically stationary state, and b) total (domain-averaged) Eulerian kinetic energy for the spin-up and one year subsequent integration. Fluctuations in the total kinetic energy are due to the random nature of the model forcing function.

A typical example of the evolution of the stream function and the corresponding relative vorticity for a fully spun-up model run are shown in Figures 3.2 and 3.3. The dominant 100–200 km scale of the turbulent flow is readily apparent in both the stream function and the relative vorticity fields. At the same time, small scale features in the relative vorticity are also apparent, indicating the wide range of length scales present in the flow.

3.3 Simulated Float Statistics

The model float data set consists of 37 floats, with float positions and velocities given once per 0.036 non-dimensional time units, or about once per day, for a total of 12.6 non-dimensional time units, or about 1.0 year. This amounts to approximately 467 non-dimensional float time units, or 450 float months. Figure 3.4 shows a spaghetti diagram of model floats where the qualitative behavior, including looped trajectories and apparently random walks, is reminiscent of that seen in the NATRE observations.

3.3.1 Mean Flow and Eddy Kinetic Energy

sf record 12, max = (1.469)   sf record 13, max = (1.708)   sf record 14, max = (1.935)

sf record 15, max = (1.779)   sf record 16, max = (1.643)   sf record 17, max = (1.542)

sf record 18, max = (1.353)
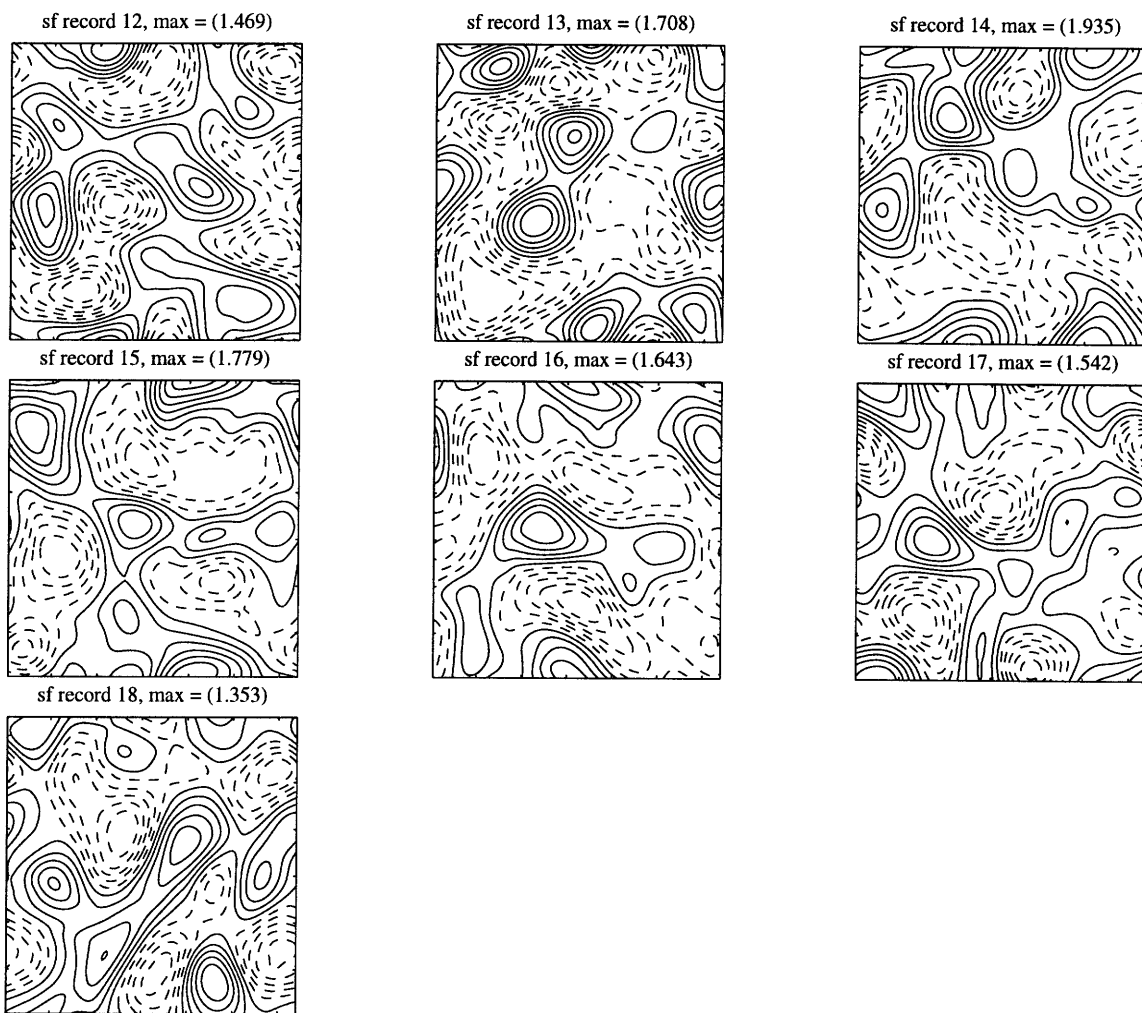
Figure 3.2: Model stream function for a typical model run showing the dominant scale of the flow. Successive frames from left to right, top to bottom correspond to intervals of 1 non-dimensional time unit, or approximately one month. Each frame represents an area of $2\pi \times 2\pi$ non-dimensional units, or 628×628 km^2.

rv record 12, max = (14.81)

rv record 13, max = (17.33)

rv record 14, max = (15.77)

rv record 15, max = (13.58)

rv record 16, max = (13.52)

rv record 17, max = (18.72)

rv record 18, max = (13.87)
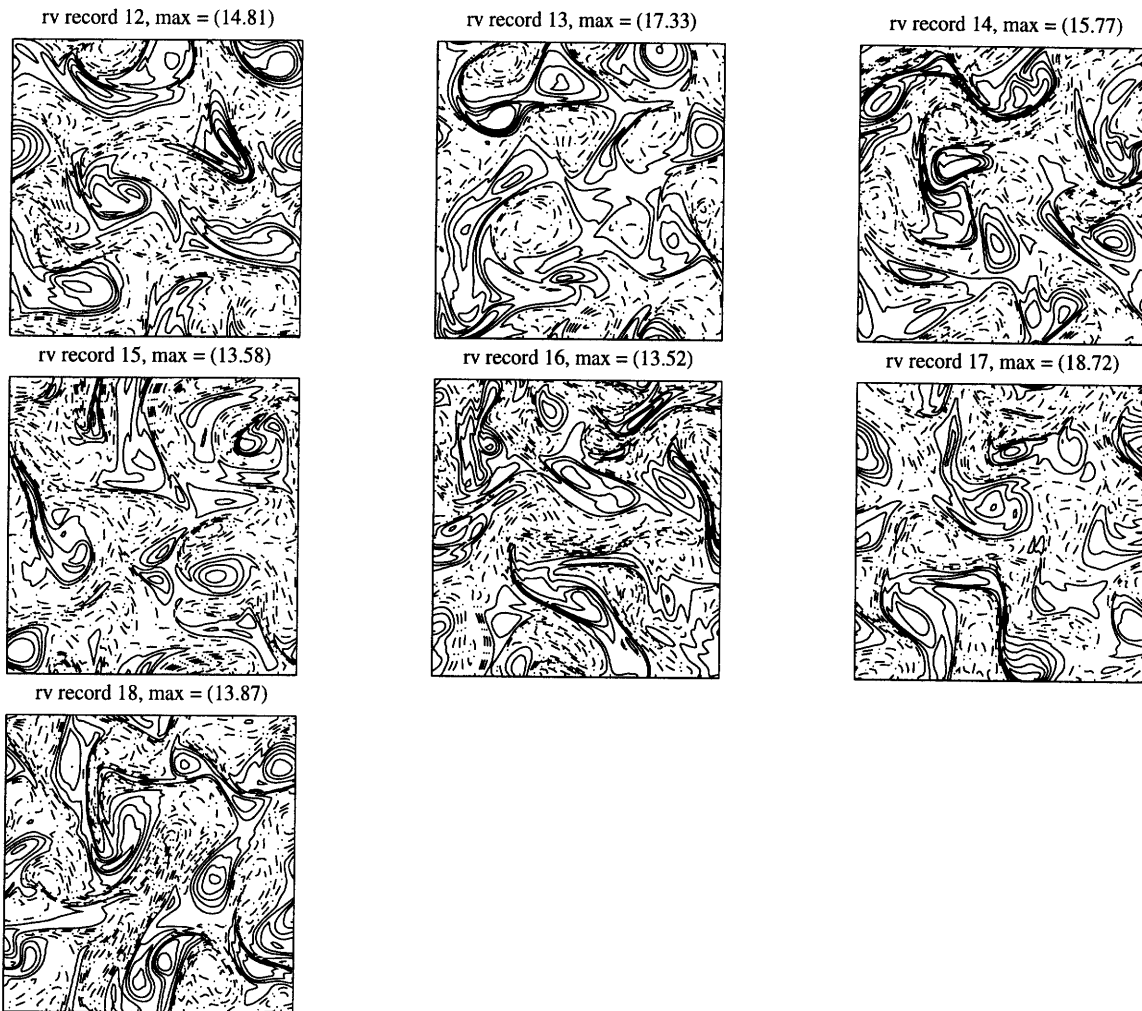
Figure 3.3: Model relative vorticity for a typical model run showing both large and small-scale structure present in the flow (displayed in the same format as Figure 3.2).

Model float trajectories
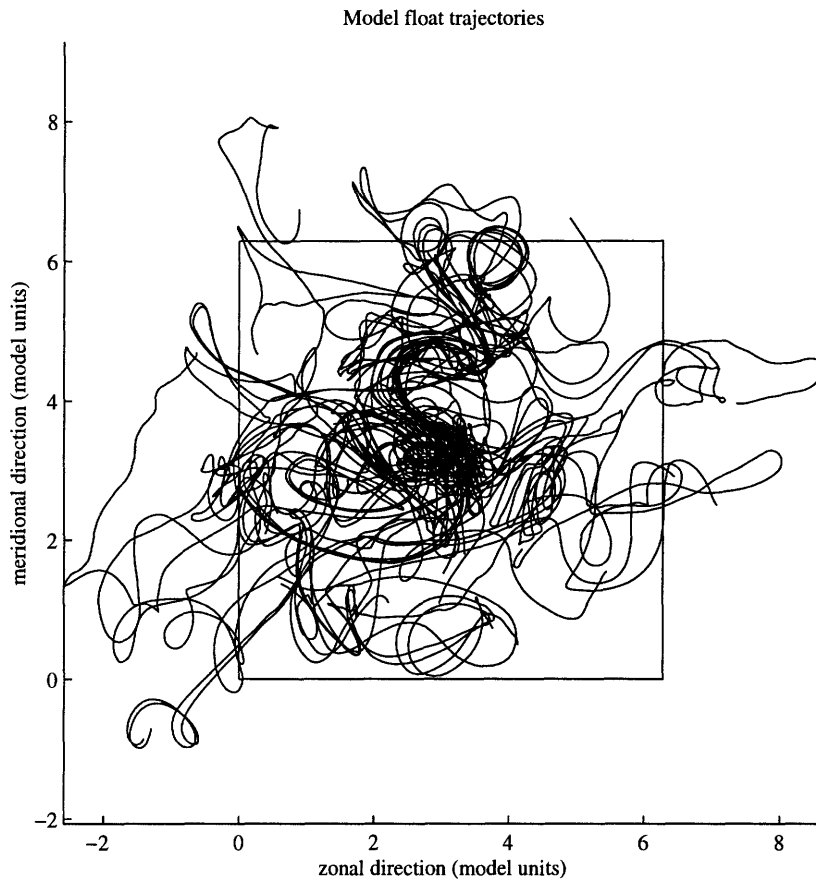
Figure 3.4: Model float trajectories for a typical model run showing loops and apparently random walks which are reminiscent of those seen in Figure 2.5. The $2\pi \times 2\pi$ (about 628×628 km^2) doubly periodic domain is marked by the square within the figure, with float tracks extending beyond the domain limits representing those which "wrapped around" the model domain.

Mean transport velocities and ensemble-averaged eddy kinetic energy were computed from model floats in the same manner as was done for NATRE floats. In the typical model run, mean transport velocities are $u_{(1,2)} = (-0.08 \pm 0.77, 0.00 \pm 0.73)$ non-dimensional units for the (eastward, northward) components, where the errors are computed as in chapter 2. The model floats thus indicate zero mean flow, as expected given the initial condition and forcing used. The (eastward, northward) combined time and ensemble-averaged EKE for the typical run are $(0.55 \pm 0.55, 0.50 \pm 0.49)$ non-dimensional units, or approximately $(8.8 \pm 8.8, 8.0 \pm 7.84)$ cm^2s^{-2}, where errors are again as in chapter 2. (The large variances here are likely related to the short time scales of the barotropic model.) These estimates of model EKE are within 10% of the EKE computed from the NATRE floats, thus indicating that the first criterion for model calibration has been satisfied.

3.3.2   Spatial and Lagrangian Auto-Correlation Functions

The length and time scales of the typical run were estimated from the SCF and LACF computed from model floats. The isotropic transverse and longitudinal SCF as computed from model floats are plotted in Figure 3.5 along with the number of float pairs available for a given separation distance. The model SCF is similar to that of the SCF computed from the observations (see Figure 2.10), with the transverse SCF having a first zero crossing of approximately 0.8 non-dimensional units, or about 80 km. This is consistent with the 70 km scale estimated in chapter 2 for the observations in the NATRE region.

Zonal and meridional LACF computed for the typical model run are plotted in Figure 3.5 along with the number of floats (constant in the model) used for a given time lag. A slight anisotropy similar to that seen in the observations (see Figure 2.10) is readily apparent, with the meridional LACF showing a small negative lobe after its first zero crossing. The zonal and meridional LACF have their first zero crossings at approximately 0.9 and 0.6 non-dimensional units, or 26 and 16 days, respectively. As shown in Figure 3.5, the integral of the LACF becomes saturated for τ less than about 1.0–1.5 non-dimensional units for the zonal correlation function, and $2.5 - 3.5$ non-dimensional units for the meridional correlation function, or about 30–40 days and 70–100 days respectively. The zero crossings are in agreement with estimates made in chapter 2 from the NATRE observations for the zonal correlation functions and are about 25% smaller for the meridional correlation function.

45

Spatial Correlation Function for model floats (binsize = 0.1473)

(a)

$S_{ii}(\xi)$

— transverse
--- longitudinal

# of float pairs

separation distance, ξ (model units)

Lagrangian Auto–Correlation Function for model floats

(b)

$R_{ii}(\tau)$

— zonal
--- meridional

time lag, τ (model time units)
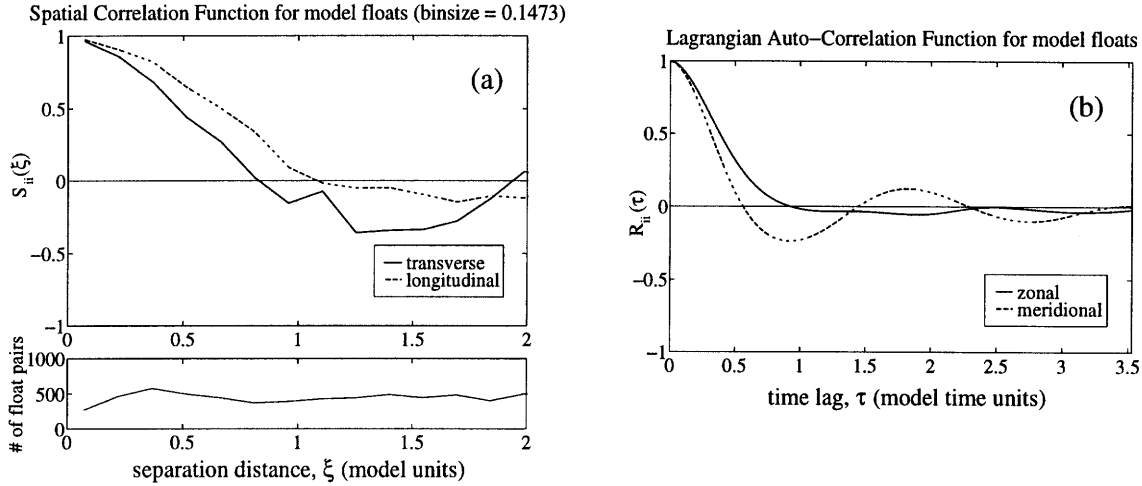
Figure 3.5: a.) Transverse (solid line) and longitudinal (dashed line) spatial correlation functions computed from model floats along with the number of float pairs used for a given separation distance. The calculated covariances were averaged over 0.15 non-dimensional units (about 15 km) bins of separation distance. b.) Ensemble averaged zonal (solid line) and meridional (dashed line) Lagrangian auto-correlation functions computed from model floats. The number of floats used for a given time lag is 37.

At this point, excepting to some degree the model time scales, the model has been "well calibrated" according to the three criteria outlined above.[2]

3.4 Simulated Tracer Fields

Next, a typical tracer dispersal simulation is examined in order to assess qualitative and quantitative agreement with both the NATRE tracer data and the theoretical predictions of chapter 1. A qualitative description is given of a simulated localized release of passive tracer. The area and concentration of model tracer is compared to the theoretical predictions discussed in chapter 1 and to the observations discussed in chapter 2. Finally, the relationship between model rms tracer streak width, rms strain rate, and explicit small-scale diffusivity is examined, along with possible biases and uncertainties associated with the measurement of these quantities.

---

[2]See Appendix B for a discussion of the discrepancy between model Lagrangian time scales and those estimated from the NATRE observations.

3.4.1 Tracer Dispersal

Model tracer was released simultaneously with the model floats into the fully spun-up turbulent flow. The initial tracer distribution was a Gaussian patch,

$$\theta(x, y, t_o) = e^{[(x-x_o)^2+(y-y_o)^2]/(2\sigma)^2} \tag{3.11}$$

of radius $2\sigma = 0.2$ non-dimensional units, or 20 km, released at the center of the model domain, thus making it about the same size and location as the model float array (numerical resolution considerations required the diameter of the initial distribution to be about twice as large as the initial NATRE distribution). To make the total tracer inventory in the model correspond to that of NATRE (139 kg), the appropriate redimensionalization is 2.67 kg/(non-dimensional unit).

The evolution of the model tracer field for the typical model run is shown in Figure 3.4.1 (the corresponding stream function and relative vorticity for this realization are shown in Figures 3.2 and 3.3, respectively). For comparison, the model float positions for this run are also plotted in frame-by-frame format in Figure 3.7. By overlaying the floats and tracer, it can be seen that the two are advected together. That is, higher concentrations of model floats are generally accompanied by higher concentrations of tracer, as expected for simple advection. On rare occasions, however, when a float accompanies a thin tracer streak of low concentration, diffusion may cause the tracer concentration to fall below the detectable threshold (in this case, the lowest contour interval).

Qualitatively, the dispersal of model tracer is consistent with both theoretical expectations and observations from NATRE. Immediately after release, there is a pronounced period of streak formation, characterized by a fairly well defined streak width. For longer times, the streaks begin to wrap around one another and merge, gradually filling in the model domain (the tracer concentration and area is not considered for times greater than about 6 non-dimensional time units, or about 6 months, when the tracer has significantly "wrapped around" the periodic model domain). For a two dimensional fluid, the strain tensor may be diagonalized yielding $\gamma = \sqrt{\psi_{xy}^2 + \frac{1}{4}(\psi_{xx} - \psi_{yy})^2}$. Using the model stream function and averaging over the entire model domain, the rms strain rate for the typical model run is $\gamma \approx 2.5$ non-dimensional units, or about 1×10^{-6} s^{-1}. This value is about three times larger than that estimated by Ledwell et al. (1993) for the NATRE region (the larger strain rate in the model is consistent with the shorter time scales of a barotropic verses baroclinic dynamics). Given this slightly larger rms strain rate, as well as the larger

record 12, (max = 1)   record 13, (max = 0.402)   record 14, (max = 0.2029)

record 15, (max = 0.1392)   record 16, (max = 0.1056)   record 17, (max = 0.08878)

record 18, (max = 0.06751)
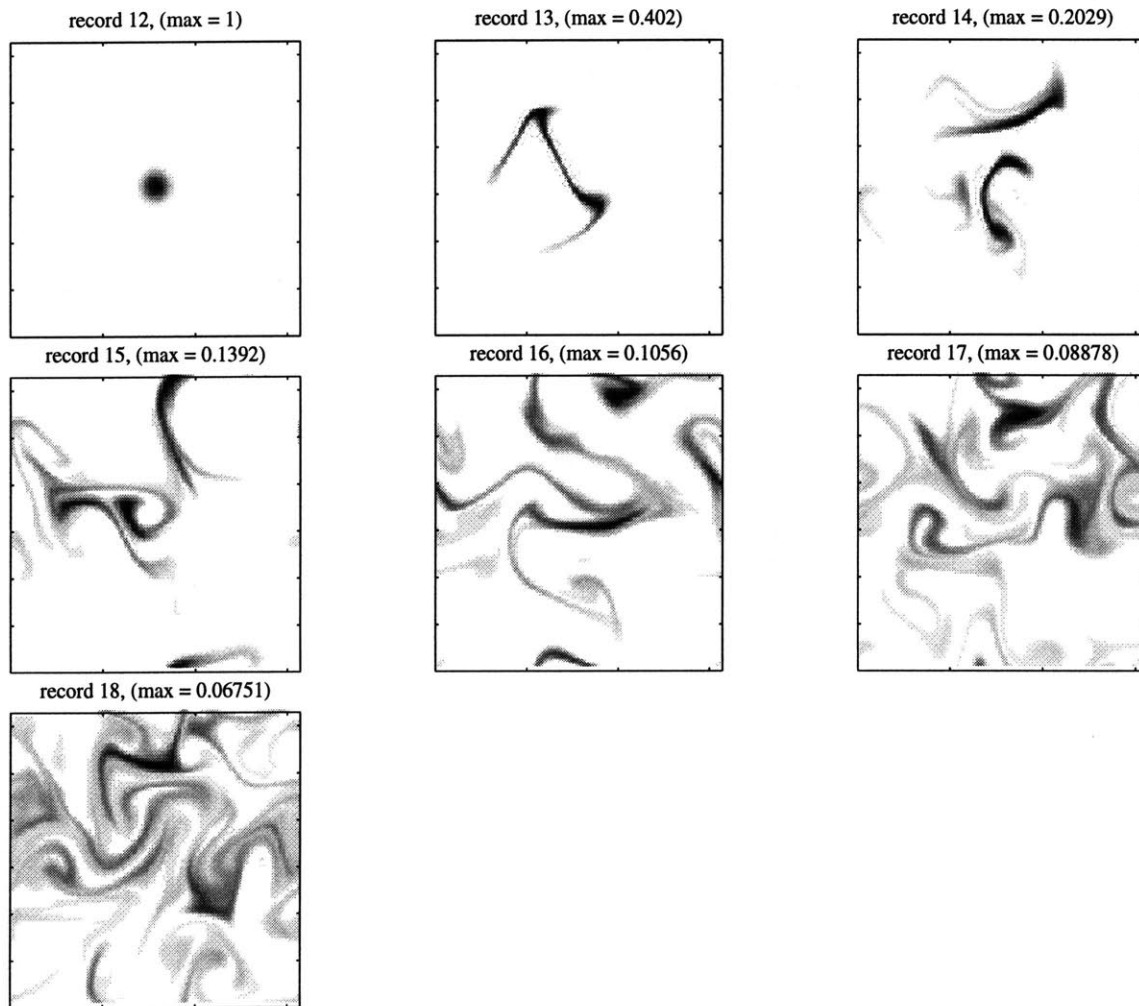
Figure 3.6: Model tracer for a typical model run showing the rapid streak formation followed by the gradual "filling in" of tracer (displayed in the same format as Figure 3.2).
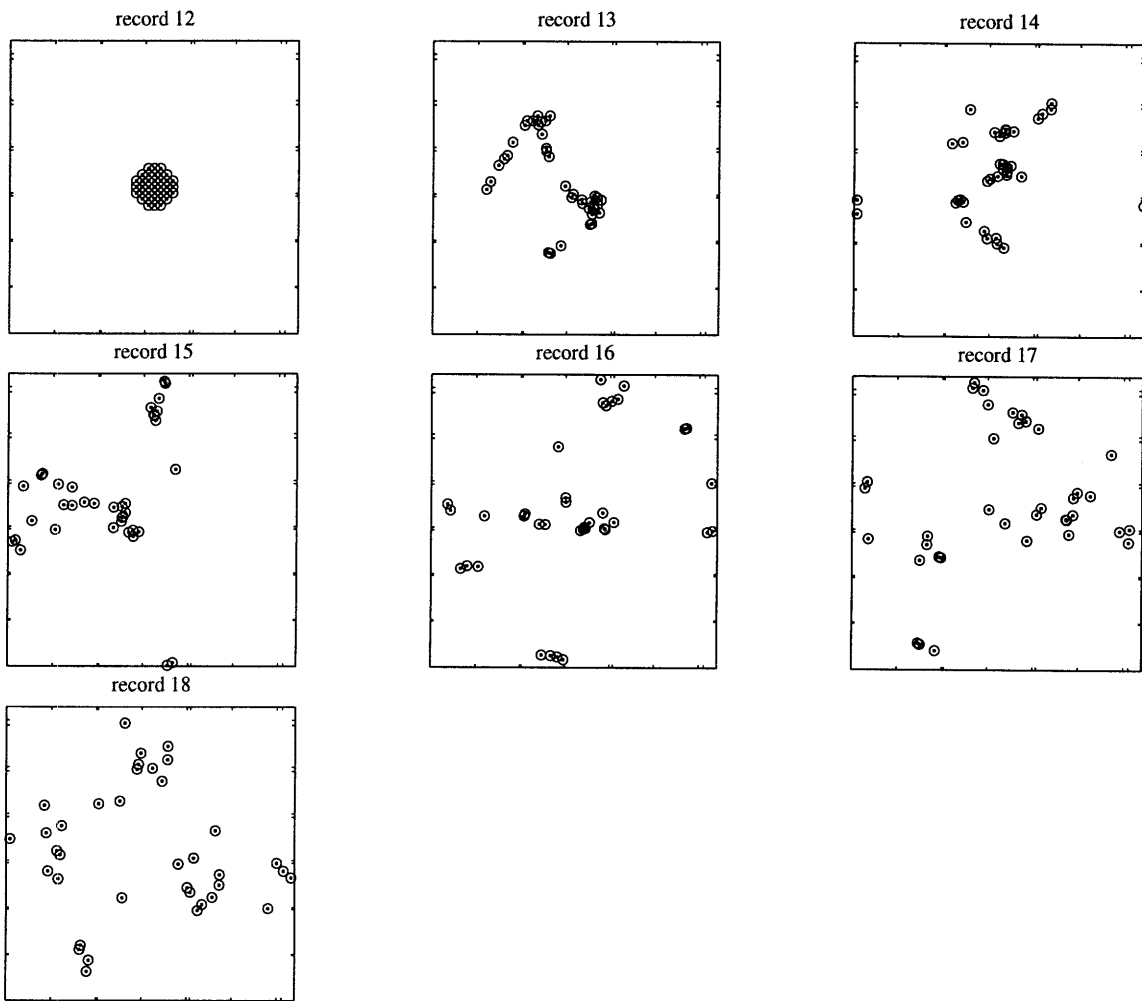
Figure 3.7: Model floats for a typical model run showing similar advection patterns as model tracer of Figure 3.6 (displayed in the same format as Figure 3.2). In general, higher concentrations of model floats are accompanied by higher concentrations of tracer, as expected for simple advection. On rare occasions, however, when a float accompanies a thin tracer streak of low concentration, diffusion may cause the tracer concentration to fall below the minimum detectable level.
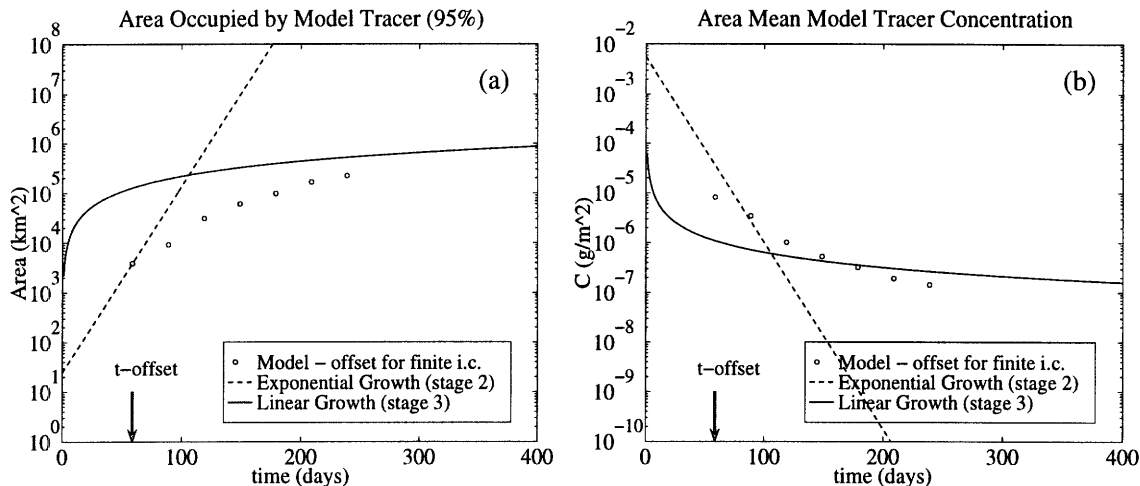
Figure 3.8: Exponential (dashed lines) and linear (solid lines) growth phases (stages 2 and 3 of section 1.2) of a) tracer area and b) mean concentration for a theoretical point release of passive tracer in a turbulent flow and model results (open circles) for the seven frames in Figure 3.6. Theoretical curves are for $\kappa_e = 1 \times 10^3$ m^{2}s^{-1}, $\kappa_s = 10.0$ m^{2}s^{-1}, $\gamma = 1.0 \times 10^{-6}$ s^{-1}, and $\alpha = 1$. Model results are plotted with a time offset of approximately 73 days to compensate for the finite size of the initial release.

small-scale diffusivity in the model compared to the NATRE experiment (which was necessary in order to resolve the tracer streaks), the model tracer was expected to disperse more rapidly than the NATRE tracer, which it did. This can be confirmed by comparing frames five and six of Figure 3.4.1 to the observed NATRE tracer distribution from Fall, 1992 in Figure 2.1 (note that the model domain in Figure 3.4.1 corresponds to an area about 4 times that sampled in the NATRE experiment in Fall, 1992).

3.4.2   Tracer Area and Concentration

Next, the quantitative agreement between the theoretical predictions of chapter 2 and the model tracer dispersal is assessed. As was done for the NATRE observations in chapter 2, the model tracer dispersal was assumed isotropic with a characteristic large-scale eddy diffusivity of $\kappa_e = 1$ m^{2}s^{-1}. For the typical model run with explicit small-scale diffusivity, $\kappa_s = 10.0$ m^{2}s^{-1}, and rms strain rate, $\gamma = 1.0 \times 10^{-6}$ s^{-1}, and assuming a coefficient for the exponential growth phase, $\alpha = 1$, the theoretical curves for tracer area and concentration (equations (1.3) – (1.6)) are shown in Figure 3.8. Also plotted in these figures are the model tracer area and concentration for the tracer distributions shown in

50

Figure 3.4.1. As was done for the NATRE data in chapter 2, the model data points are plotted with a time offset based upon the predicted growth rates and the initial area of the model tracer patch. For these parameter values, the time offset is approximately 73 days. Comparing the numerical results with the theoretical predictions, poor agreement is found for the exponential growth phase, although a tendency toward the linear regime is apparent for large times. Of notable interest, however, is that re-plotting the theoretical curves using a smaller value for the exponential growth coefficient, say $\alpha = .4$ (Figure 3.9), results in a marked improvement in the agreement between the numerical results and the theoretical predictions (note this changes the time offset for the model data points to approximately 142 days). This improvement may be interpreted in two ways. Either the order-one coefficient for the exponential growth phase using the rms strain rate has an actual value of approximately $\alpha \approx .4$, or this coefficient is closer to $\alpha \approx 1$ but because of the time dependence, some other quantity (which may be closely related to the rms strain rate, γ) really governs the exponential phase of the tracer dispersal. Considering the results of experiments described in the next section, it appears that for a strictly *steady* strain rate in fact $\alpha \approx 1$. However, for the case of an unsteady strain rate, one expects on theoretical grounds that spatial and temporal variations in the strain rate should effect the tracer area and concentration in a nonlinear fashion, *i.e.*, the theoretical balance, $\sigma_s = \sqrt{\kappa_s/\gamma}$, should really only apply for a steady strain rate. Indeed it is possible that the quantity computed by Ledwell *et al.* (1993) from the observed length of the NATRE tracer streaks is not rigorously the rms strain rate, but rather the more relevant quantity pertaining to the unsteady problem. This would also be consistent with the close agreement found in chapter 2 between the NATRE tracer and theoretical predictions with $\alpha = 1$. This hypothesis is further discussed in the next section and in chapter 4.

3.4.3   Streak Width and Small-Scale Diffusivity

The model tracer fields are now examined to determine the relationship between the rms streak width, the rms strain rate and the explicit small-scale diffusivity. The specific goal is to test (or calibrate) the theoretical prediction that $\sigma = \sqrt{\kappa_s/\gamma}$.

Taken as an example was the tracer distribution of Figure 3.4.1, frame 6, which corresponds to approximately 5 months since release. Tracer streaks were sampled by taking cross-sections of tracer concentration at 10 arbitrarily chosen locations. The locations of these sections along with the corresponding cross-streak concentration are shown in Figure

51

Area Occupied by Model Tracer (95%)

○ Model – offset for finite i.c.
--- Exponential Growth (stage 2)
— Linear Growth (stage 3)

Area (km^2)

t–offset

(a)

time (days)

Area Mean Model Tracer Concentration

○ Model – offset for finite i.c.
--- Exponential Growth (stage 2)
— Linear Growth (stage 3)

C (g/m^2)

t–offset

(b)

time (days)
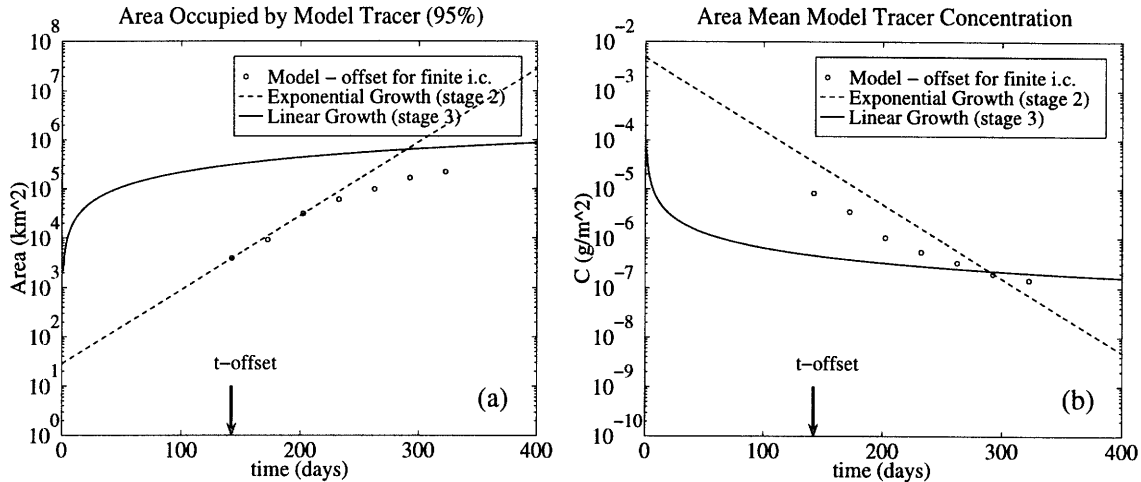
Figure 3.9: Same as figure 3.8 except with $\alpha = .4$ and a time offset for model results of approximately 142 days.

3.10. As is apparent in the un-normalized cross-streak profiles, a wide range of absolute concentrations are represented in this particular sample, with nearly an order of magnitude difference between the largest and smallest cross-streak peak concentrations. Normalizing these cross-streak profiles by their peak concentration shows that their structure is quite similar, suggesting a fairly well defined rms streak width. For this particular sample, the estimated rms streak width is $\sigma \approx 10$ km. Assuming that the along-streak strain is balanced by cross-streak diffusivity, i.e., $\sigma = \sqrt{\kappa_s/\gamma}$, would yield an effective small-scale lateral diffusivity, $\kappa_s \approx 100$ m^{2}s^{-1}. This value is an order of magnitude larger than the explicit small-scale diffusivity actually set in the model. That is, the actual streaks are considerably wider than predicted by this theoretical balance. This discrepancy between the actual and predicted streak widths is one of the most interesting results of this study, and is analyzed in the remainder of this section.

Numerical Resolution and Sensitivity

Experiments were run to determine whether the model could indeed verify the predicted balance between the rms strain rate and the small-scale diffusivity, i.e., $\sigma = \sqrt{\kappa_s/\gamma}$. A pure, *steady* strain field, $\psi = -\gamma xy$, was constructed in which γ was set equal to the rms strain rate of the "typical" model run. It was found that the steady streak width in these experiments was well predicted (to within about 10% – 20%) by the rms strain rate and small-scale diffusivity when the streak was well resolved in the model (*i.e.*, 10 grid points

52
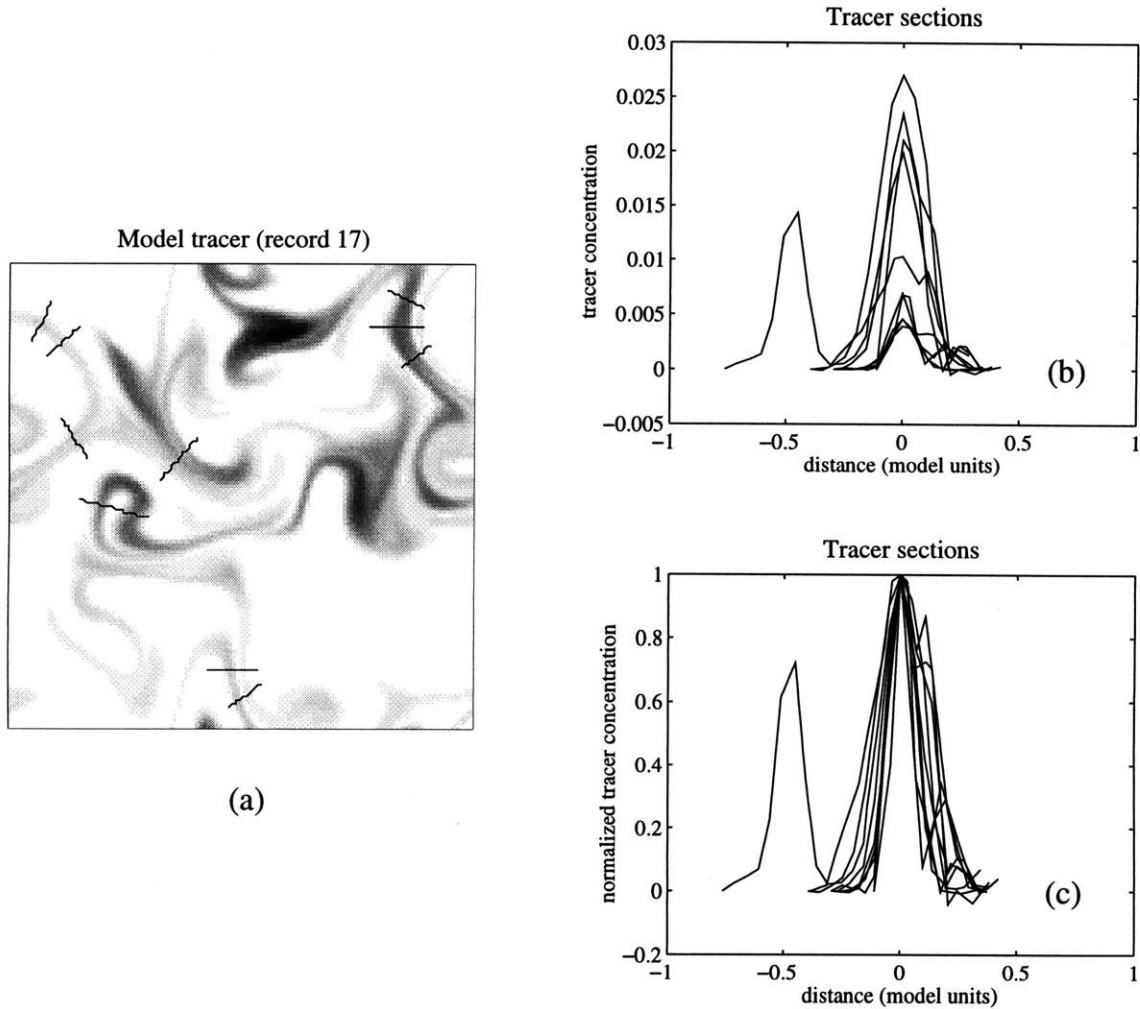
Figure 3.10: Cross-streak profiles of model tracer showing a "well defined" rms streak width. a) The model tracer distribution is the same as in frame 6 of Figure 3.6, corresponding to approximately 5 months since release. Solid lines represent the locations of tracer sampling sections (waviness in the section lines is an artifact of the discrete sampling and the model grid, *i.e.*, no interpolation was done along the sections). b) Absolute and c) normalized concentrations along the sections are plotted so that the local maximum concentration is centered at zero.

or more wide). Furthermore, increasing κ_s by a factor of 4 showed that the streak width increased correspondingly by a factor of 2, in agreement with the expected theoretical dependence. For a poorly resolved streak, for example, one which was only 5 grid points wide, the error on the predicted streak width increased to nearly 60% and thus κ_s would have be over-estimated by a factor of 2.5. These experiments demonstrate that the theoretical relation $\sigma = \sqrt{\kappa_s/\gamma}$ holds true in the model for a well resolved tracer streak, while an unresolved streak will be wider than predicted because of numerical diffusion.

Time-Dependent Effects

That the theoretical relation for the steady case is reproduced by the model only for well resolved tracer streaks led me to suspect that time dependence in the model might be causing a "numerical bias" towards wider streak widths. Specifically, because of the variance in the strain rate, individual streaks in the model may occasionally become narrow enough to push the limits of model resolution, biasing the tracer towards larger streak widths.

To determine whether model streak width varied as $\sigma = \sqrt{\kappa_s/\gamma}$ for an unsteady strain rate, The model was re-run using the parameter settings of Table 3.1, increasing κ_s by a factor of four in one case, and decreasing κ_s by a factor of four in a second case. These experiments showed that increasing κ_s by a factor of 4 resulted in an factor of 1.6 increase in streak width, while decreasing κ_s by a factor of 4 resulted in a 1.5 factor decrease in streak width. In other words, although the streak width was found to be dependent on the small-scale diffusivity, this dependence was not as great as it was in the experiments using a pure, steady strain (*i.e.*, a factor 1.5 change instead of the previous factor 2 for resolved streaks). One explanation for this weak dependence of model streak width is the time-variability of the strain rate. To examine this possibility, the rms streak width from a typical model run was compared to the streak width obtained from a steady strain rate experiment (as described above) which used the same small-scale diffusivity and strain rate (*i.e.*, the steady strain rate was equal to the rms strain rate of the unsteady experiment). Tracer streaks in the unsteady experiment were generally wider than for the steady case with even the narrowest streaks in the unsteady case being as much as $1\frac{1}{2}$ times wider than those of the steady case. Keeping in mind a possible bias due to streak merging (see below), this implies that for this particular model resolution and choice of parameters such a numerical bias could account for about a factor of 3 difference between the predicted and the actual small-scale diffusivity in this model tracer release experiment. With respect to the analysis

54

of tracer area and concentration given in the previous section, this difference may also account for the adjusted coefficient, $\alpha = .4$, for the exponential phase of tracer dispersal. Additional effects of the variability of the rms strain rate in terms of the non-linearity of the relationship, $\sigma = \sqrt{\kappa_s/\gamma}$ may further bias estimates of κ_s (remember that this relationship assumes a steady strain rate), however, this problem has not been addressed here, and will thus only be briefly discussed in chapter 4.

Merging Bias

A closer analysis of the tracer distribution in Figure 3.10 shows that some of the sampled streaks are actually multiple streaks which have been stirred together by the large scale motion and then merged by diffusion. Once this merging has occurred, the individual streaks lose their identity, thus leaving a single streak which is wider than any one component streak. The inability to distinguish individual streaks from those which have resulted from a recent merger of streaks can thus lead to a bias towards wider estimated rms streak width. For the example shown in Figure 3.10, this "merging bias" has led to the over-estimation of the streak width by approximately a factor of 2 (estimated by eye) and thus the small-scale diffusivity by a factor of 4. This factor of 4 taken together with the factor of 3 estimated "numerical bias" due to the time dependence and numerical resolution, readily accounts for the order of magnitude discrepancy in the example model run between the explicit small-scale diffusivity and that estimated from the rms strain rate and streak width.

Explicit small-scale motions

An additional hypothesis tested was that the explicit small-scale motions (*i.e.*, small-scale stirring) in the model, enhanced the rate of tracer dispersal on similar scales, so that the sub-gridscale diffusivity, κ_s, was not the only mechanism working to set the cross streak width. To test this, the model was re-run with the parameter settings of Table 3.1 but using a high-pass filtered flow field (removing wavelengths greater than about .4, or 40 km) to advect the tracer. The resulting tracer concentration and streak width was found to differ from the standard run by no more than a few percent, indicating that explicit small-scale motions in the model do not significantly contribute to the discrepancy in question.

Chapter 4

Summary and Remarks

The overall goal of this study was to characterize isopycnal mixing and stirring of passive tracer in the open ocean. I examined the statistics of the NATRE float data, and used a numerical model to estimate the biases and uncertainties associated with estimates of the small-scale diffusivity, the rms strain rate, and the large-scale effective eddy diffusivity made from the NATRE tracer observations. Particle statistics were computed from the float data in order to characterize the kinematics of the mesoscale flow. A barotropic vorticity model was then used to simulate the stirring and mixing of a passive tracer in a turbulent flow. The model was calibrated so that the statistics of model floats agreed as closely as possible with those computed from the NATRE floats based on the EKE, characteristic length and integral time scales, and the approximate degree of anisotropy due to planetary β. The rate of dispersal of model tracer was then examined in order to assess qualitative and quantitative agreement with the NATRE observations and theoretical predictions.

The effective eddy diffusivity computed from the NATRE float data was found to be roughly consistent with that estimated from the tracer data. Given the uncertainties associated with the float calculations, the estimate $\kappa_e \approx 1 \times 10^3$ m^{2}s^{-1} determined from the tracer distribution for Spring, 1993 and Fall, 1994 (Ledwell, personal communication) should be accurate to within about a factor of 2.

Passive tracer dispersal in the barotropic vorticity model was qualitatively consistent with observations from the NATRE field experiment and theoretical growth rates of tracer area and concentration. However, quantitative analysis of model tracer streaks formed by the mesoscale strain field indicated that the estimation of small-scale diffusivity, κ_s, from

the predicted balance $\sigma_s = \sqrt{\kappa_s/\gamma}$, can lead to both observational and numerical biases resulting in the over-estimation of κ_s. Of particular relevance to the NATRE experiment is the possible bias toward larger estimated rms streak width due to the inability of the observer to distinguish individual streaks from those which have resulted from a recent merger of streaks. This bias could lead to the over-estimation of κ_s by up to a factor of 2 to 4, implying that the estimate of κ_s made by Ledwell et $al.$, (1993) from the NATRE tracer observations has an associated uncertainty of similar magnitude.

Of additional interest is the unexplained two orders of magnitude discrepancy between the effective small-scale diffusivity estimated by Ledwell et $al.$, (1993) from the NATRE tracer observations and that estimated by Young et $al.$, (1982) due to shear dispersion by internal waves. As noted earlier, this discrepancy implies the presence of a highly efficient mixing process acting at scales of order $1 - 10$ km (Ledwell, personal communication). Based on numerical simulations, it appears that explicit small-scale motions, at least in the barotropic vorticity model used here, have a negligible effect on the mixing ($i.e.$ the small-scale stirring) of passive tracer, and hence can not account for such an enhanced diffusivity. (Although these experiments did not explicitly resolve such small scales, the model dynamics render it unlikely that increasing the model resolution would change this result.) Whether the large rate of dispersion observed during the NATRE experiment was due to a vertical shear associated with the mesoscale motion, or whether it was due to some other mechanism remains to be seen.

A problem which has only partially been addressed in this study, but which warrants further attention is that the mesoscale stirring of tracer in the ocean is governed by a strain rate which varies in time and space. If one assumes, for example, that the streak width is given locally by the steady balance, $\sigma_s = \sqrt{\kappa_s/\gamma}$, and further that γ has an associated probability distribution, $\langle\gamma\rangle$, it is apparent that the probability distribution of the streak width, $\langle\sigma\rangle \neq \sqrt{\kappa_s/\langle\gamma\rangle}$. Dispite this, as was shown in chapter 3, the period of rapid streak formation in the model tracer can be at least qualitatively described by exponential growth. It is likely, however, that in the case of an unsteady strain rate estimates of small-scale diffusivity from the steady balance, $\sigma = \sqrt{\kappa_s/\gamma}$, will be biased high, and that the unsteady problem strictly requires a modified version of this balance. For the numerical experiments done in this study, the biases in the unsteady problem were primarily due to streak merging and numerical effects, and hence the details of this theoretical bias were not adequately assessed. Further investigation of the unsteady problem using higher resolution simulations is a subject of ongoing research.

Finally, it is worthwhile to say a few general words about the use of barotropic vorticity models to study of the dispersion of passive tracer in the ocean. As revealed in chapter 3, care must be taken to assess resolution requirements for numerical simulations in unsteady flows. Further, the omission of baroclinic effects in a vorticity model such as the one used in this study leads to a decrease in the characteristic time scales of the flow (see chapter 3 and Appendix B). Nevertheless, it appears that a barotropic vorticity model should be able to qualitatively, if not quantitatively, simulate the dispersal of passive tracer in the open ocean. In light of the amount of effort devoted in this study to achieving the desired length and time scales in the barotropic model, however, it seems that a $1\frac{1}{2}$ or 2 layer model would be a more natural choice for future studies of tracer dispersal in the ocean.

Appendix A

More About the Float Data Set

The float data used in this study consisted of the ten SOFAR floats deployed during the North Atlantic Tracer Release Experiment and four (of the eighteen) SOFAR floats released during the Subduction experiment (Price *et al.*, in preparation). Each float was pre-programmed to make daily vertical excursions through a portion of the water column defined by some maximum and minimum temperature surface, T_{max} and T_{min}. On each excursion, the instrument recorded the pressure at these two temperature surfaces, and then settled for the remainder of the day to a depth corresponding to the average of the two pressure extrema. A maximum and minimum pressure, P_{max} and P_{min}, was also specified for each instrument, which served to limit the extent of its vertical excursion in the case of extreme conditions. The 10 NATRE floats were programmed for same temperature and pressures, while the four Subduction floats were programmed slightly different than one-another and to explore a shallower portion of the water column than the NATRE floats. The exact values of the pre-programmed T_{max}, T_{min}, P_{max}, and P_{min} for the NATRE floats are summarized in Table A.1. The life-span of the NATRE and selected Subduction floats is shown in Figure 2.4 in the main text.

A.1 The NATRE Floats

Of the 10 NATRE floats, all provided reasonable velocity data during the time that they were transmitting, however, two of the floats, tr60 and tr64, apparently experienced

Float #	T_{max}	T_{min}	P_{min}	P_{max}	Mean depth
tr55	16.32 C	15.12 C	120 Dbar	550 Dbar	295 m
tr56	16.32 C	15.12 C	120 Dbar	550 Dbar	295 m
tr57	16.32 C	15.12 C	120 Dbar	550 Dbar	295 m
tr58	16.32 C	15.12 C	120 Dbar	550 Dbar	295 m
tr59	16.32 C	15.12 C	120 Dbar	550 Dbar	295 m
tr60	16.32 C	15.12 C	120 Dbar	550 Dbar	295 m
tr61	16.32 C	15.12 C	120 Dbar	550 Dbar	295 m
tr62	16.32 C	15.12 C	120 Dbar	550 Dbar	295 m
tr63	16.32 C	15.12 C	120 Dbar	550 Dbar	295 m
tr64	16.32 C	15.12 C	120 Dbar	550 Dbar	295 m
sb14	16.50 C	15.30 C	100 Dbar	550 Dbar	285 m
sb15	20.00 C	18.00 C	90 Dbar	500 Dbar	155 m
sb19	20.00 C	17.50 C	90 Dbar	350 Dbar	170 m
sb26	20.00 C	17.50 C	90 Dbar	400 Dbar	170 m

Table A.1: Programming information for NATRE and selected Subduction floats. For each float, the maximum and minimum temperature is given along with the limiting pressure surfaces of its vertical excursion. Mean depths are estimated based on the programmed temperature and XBT profiles taken during the Subduction mooring deployment cruises (Trask and Brink, 1993).

failure of either their pressure or temperature sensors (Price *et al.*, in preparation). Judging by the trajectories of these two floats (these are the two whose year long trajectories appear to the east of the NATRE injection site in Figure 2.5), it may be that they settled at a deeper level than did the other floats, and therefore were advected eastward instead of westward with the rest of the floats. Based on EKE's computed from individual float records (Table A.2), however, it does not appear that the two floats in question were in a less energetic portion of the water column, as would be expected if they were much deeper.[1] Since it is equally possible that these two floats were advected eastward merely because they sampled a local flow feature, they are retained in the statistical analysis in chapter 2, despite the apparent malfunction of some component of their temperature or pressure sensors. In any event, only the mean velocities and not the EKE measured by these floats were different than the other floats, so that even if these floats were deeper, the main results of this study would not be effected.

---

[1]Current meter records from the central Subduction mooring show a strong vertical coherence of direction and amplitude of horizontal velocity between 200 m and 750 m, with a decrease in vertical coherence and EKE occurring below 1500 m (see Brink *et al.*, 1993).

Float #	Float days	mean u $\frac{cm}{sec}$	mean v $\frac{cm}{sec}$	EKE_u $\frac{cm^2}{sec^2}$	EKE_v $\frac{cm^2}{sec^2}$	EKE_{total} $\frac{cm^2}{sec^2}$
tr55	3	-1.4 ± 2.8	1.3 ± 4.1	0.4 ± 1.0	1.2 ± 4.1	1.6 ± 2.1
tr56	117	-3.6 ± 1.2	-0.7 ± 1.2	3.6 ± 1.8	4.5 ± 2.1	8.1 ± 1.8
tr57	7	-3.8 ± 9.3	-1.4 ± 3.5	12.7 ± 22.0	2.2 ± 4.1	14.9 ± 22.3
tr58	374	-1.1 ± 0.6	-1.5 ± 0.6	2.9 ± 1.1	4.1 ± 1.7	7.0 ± 1.5
tr59	116	0.8 ± 0.7	0.0 ± 0.6	1.2 ± 0.4	1.2 ± 0.7	2.4 ± 0.5
tr60	336	0.4 ± 0.8	0.0 ± 0.4	4.8 ± 1.4	1.3 ± 0.4	6.0 ± 1.3
tr61	215	-0.3 ± 0.8	-0.5 ± 0.5	3.1 ± 1.3	1.4 ± 0.5	4.5 ± 1.4
tr62	364	0.9 ± 0.7	-0.3 ± 0.5	3.9 ± 1.2	2.1 ± 0.7	6.0 ± 1.2
tr63	3	-0.5 ± 2.1	-0.4 ± 1.4	0.3 ± 0.6	0.1 ± 0.3	0.4 ± 0.7
tr64	192	-3.3 ± 0.9	-0.9 ± 0.9	3.6 ± 1.9	4.8 ± 2.1	8.4 ± 1.9
sb14	383	-1.7 ± 1.2	-0.3 ± 0.9	13.2 ± 4.9	9.0 ± 3.3	22.2 ± 5.3
sb15	741	-1.4 ± 0.7	-1.0 ± 0.7	7.3 ± 1.7	10.3 ± 2.3	17.5 ± 2.2
sb19	728	-1.3 ± 0.9	-1.6 ± 0.9	12.5 ± 3.4	15.0 ± 3.5	27.5 ± 3.8
sb26	666	-2.1 ± 0.8	-1.0 ± 0.7	9.2 ± 2.4	10.0 ± 5.1	19.2 ± 4.1

Table A.2: Mean velocity and EKE statistics for individual floats.

A.2 The Subduction Floats

The four Subduction floats used in this study were advected through the site of the NATRE experiment and were programmed to explore a slightly shallower region of the water column than the NATRE floats (Table A.1). Based on XBT profiles taken during the Subduction mooring deployment cruises (Trask and Brink, 1993), the average depth of the NATRE floats was approximately 295 m, while the average depths of Subduction floats sb14, sb15, sb19, and sb26 were 285 m, 155 m, 170 m, and 170 m, respectively. Of obvious concern regarding inclusion of the shallower Subduction floats in the analysis of chapter 2 was that they may have biased the statistics. To determine the extent of this, mean velocities and EKE of each of the NATRE and Subduction floats were computed independently (Table A.2). The mean velocities of the Subduction floats were not apparently different from the NATRE floats, however the EKEs of the Subduction floats were about 2 – 3 times greater. The latter discrepancy may be due in part to the fact that the Subduction floats were shallower than the NATRE floats and thus were in a more energetic part of the water column. This, however, would not explain why the deeper of the four Subduction floats, sb14, which was at approximately the same depth as the NATRE floats, was equally as energetic as the three shallower Subduction floats. An alternative explanation is that the Subduction floats sampled a more energetic region laterally than the NATRE floats. Velocity stick plots from current meters from the five Subduction moorings (see Brink *et al.*, 1993) indeed suggest that the NATRE release site, located at approximately the

63

same location as the central Subduction mooring, was relatively quiescent compared the surrounding regions (the locations of the five Subduction moorings is indicated in Figure 2.1). In particular, at depths of 150 and 200 m (at which all but the south-east mooring had current meters), horizontal velocities at the central mooring were as much as 2 times smaller than at the neighboring moorings. With this in mind, and considering the near proximity of the five moorings as well as the four Subduction floats to the NATRE release site, it was deemed both useful and appropriate to include the Subduction floats in this analysis. Note, however, that even in the presence of a factor of 2 bias towards higher EKE, the major results of this study regarding the rates and uncertainties of particle and tracer dispersal would be little effected.

Appendix B

Limitations of the Barotropic Vorticity Model

A discussion of the role of barotropic and baroclinic modes in continuously stratified systems is provided. The question at hand is: How is a single homogeneous layer in a multi-layer model affected by the presence of other layers? More practically, how well can these effects be parameterized into a single barotropic layer model? The answer lies primarily in the smaller time scales and larger length scales of barotropic versus baroclinic Rossby waves, and in the role of vortex stretching in modifying the inverse energy cascade of two-dimensional turbulence.

B.1   Barotropic and Baroclinic Rossby Waves

Consider the potential vorticity equation for a continuously stratified, inviscid, hydrostatic, Boussinesq fluid on a β-plane,

$$\frac{\partial}{\partial t}\left(\nabla^2 + \frac{\partial}{\partial z}\frac{f_o^2}{N^2}\frac{\partial}{\partial z}\right)\psi + J\left(\psi, \left[\nabla^2 + \frac{\partial}{\partial z}\frac{f_o^2}{N^2}\frac{\partial}{\partial z}\right]\psi\right) + \beta\frac{\partial\psi}{\partial x} = 0. \qquad (B.1)$$

where $\psi = \frac{1}{\rho_o f_o}P$ is the geostrophic stream function, $f = f_o + \beta y$ is the linearized Coriolis parameter, and $N(z)$ is the buoyancy frequency. It is readily shown that for the linear

65

problem, the the frequency, σ_i, of the ith mode may be expressed as

$$\sigma_i = -\frac{\beta k}{k^2 + l^2 + \lambda_i} \qquad (n = 0, 1, 2, \ldots), \qquad (B.2)$$

where k and l are the zonal and meridional wavenumbers and $\lambda_i = 1/(\text{radius of deformation})^2$ for the ith mode. As discussed in Pedlosky (1987), the eigenvalues, λ_i form an increasing sequence:

$$\lambda_0 = 0 < \lambda_1 < \lambda_2 < \lambda_3 < \ldots < \lambda_{n-1} < \lambda_n < \lambda_{n+1} \ldots, \qquad (B.3)$$

i.e., higher modes have smaller deformation radii. Put another way, for the same horizontal scale, the barotropic mode has a higher frequency (smaller time scale) than the first baroclinic mode, which in turn has a higher frequency (smaller time scale) than the second baroclinic mode, etc. The same tendency is also apparent when considering the group velocity in the x-direction, c_{g_x} for the ith mode:

$$c_{g_x} = \frac{\beta(k^2 - [l^2 + \lambda_i])}{(k^2 + l^2 + \lambda_i)^2} \qquad (B.4)$$

where it can readily be seen that the speed of energy propagation is faster for the lower modes.

B.2 Vortex Stretching and the Inverse Energy Cascade

Now consider the two layer system,

$$\left[\frac{\partial}{\partial t} + \frac{\partial \psi_1}{\partial x}\frac{\partial}{\partial y} - \frac{\partial \psi_1}{\partial y}\frac{\partial}{\partial x}\right]\left[\nabla^2 \psi_1 + \frac{f_o^2}{g' H_1}(\psi_2 - \psi_1) + \beta y\right] = 0, \qquad (B.5)$$

$$\left[\frac{\partial}{\partial t} + \frac{\partial \psi_2}{\partial x}\frac{\partial}{\partial y} - \frac{\partial \psi_2}{\partial y}\frac{\partial}{\partial x}\right]\left[\nabla^2 \psi_2 + \frac{f_o^2}{g' H_2}(\psi_1 - \psi_2) + \beta y\right] = 0, \qquad (B.6)$$

where $g' = \frac{\rho_2 - \rho_1}{\rho}$ is the reduced gravity and H_i is the depth of each layer. The analogy between this system and the continuously stratified system in equation (B.1) is made apparent by relating the deformation radius in each layer as $L_{R_i} = \sqrt{g' H_i}/f_o = N H_i/f_o$ for the discrete and continuous systems, respectively (*e.g.*, Flierl, 1978). (Conventionally, the Rossby deformation radius for the two layer system is actually defined as $\sqrt{F_1 + F_2}$ which arises naturally in the linear equation for the first baroclinic mode.) In this formulation the potential vorticity in the ith layer is composed of a relative vorticity $\nabla^2 \psi_i = v_{ix} - u_{iy}$,

a planetary vorticity, and a stretching term, $\frac{f_0^2}{g'H_i}(\psi_j - \psi_i)$, $(j = 3 - i)$, where the latter is now expressed in terms of the motion of a discrete layer interface.

Assuming a length scale, L, a velocity scale, U, and an advective time scale, $T = U/L$, the above two-layer equations may be non-dimensionalized according to the scaling

$$[x, y, t, \psi_i] \sim [Lx^*, Ly^*, \frac{L}{U}t^*, LU\psi_i^*].$$

The non-dimensional two-layer equations can then be expressed as

$$\frac{\partial}{\partial t^*}\left[\nabla^2\psi_i^* - \hat{F}_i(\psi_j^* - \psi_i^*)\right] + J(\psi_i^*, \left[\nabla^2\psi_i^* + \hat{F}_i(\psi_j^* - \psi_i^*)\right]) + \hat{\beta}_i\frac{\partial\psi_i^*}{\partial x^*} = 0 \qquad (j = 3 - i),$$

(B.7)

where two important non-dimensional parameters have been identified which control the unforced potential vorticity balance:

$$\left.\begin{array}{l} \hat{F} = L^2 F = \frac{L^2}{L_R^2} \\ \hat{\beta} = \frac{L^2}{U}\beta = \frac{L^2}{L_\beta^2} \end{array}\right\}.$$

(B.8)

The first of these non-dimensional parameters determines the relative importance of vortex stretching in the total vorticity balance is determined by $\hat{F}$, which expresses the ratio of the deformation radius to the length scale of the flow, $\hat{F} = L^2/L_R^2$. Small $\hat{F}$ implies that contributions to the potential vorticity by vortex stretching due to variations of the interface are negligible, *i.e.*, the interface appears essentially rigid, and layer interactions are weak. Conversely, large $\hat{F}$ implies that vortex stretching dominates over the relative vorticity, and the layers interact strongly. (On these scales, the motion is similar in the two layers and the fluid tends to behave barotropically.) The importance of the planetary vorticity gradient is similarly determined by the non-dimensional parameter $\hat{\beta}$, which represents the importance of linear Rossby wave propagation compared to nonlinear advection. Thought of in terms of a ratio of length scales, if the scale of motion, L, is very small compared to the "arrest scale", L_β, then the fluid does not feel the planetary vorticity gradient, and advection dominates. If, on the other hand, L is very large compared to L_β, then the flow is dominated by linear Rossby wave motions.

Now, consider the effects of vortex stretching on the inverse energy cascade in two-dimensional turbulence. Suppose that at the start, the flow is such that most of the energy is contained in small scales $(L^2/L_R^2 \ll 1)$, so that the two layers are essentially decoupled. The tendency of energy to cascade to larger scales then implies that the dominant length scale of the flow will gradually increase due to non-linear interactions. In doing so the

scale of the motion will eventually become comparable to the baroclinic deformation scale $(L^2/L_R^2 \sim 1)$. As this happens, flow in the two layers will become coupled, hence providing more energy to the barotropic mode. Once this occurs, barotropic theory will apply, and the energy will be able to evolve to even larger length scales, and eventually to barotropic Rossby waves (e.g., Rhines, 1977). Thus, the non-linear interactions which occur within individual layers allow energy to be efficiently transferred among different *length* scales (in this case from smaller to larger). Furthermore, non-linear interactions between different modes of the system allow energy to be transferred among different *time* scales (in this case from larger time scales associated with baroclinic Rossby waves to smaller time scales associated with barotropic Rossby waves).

B.3   Implications to Barotropic Vorticity Models

In parameterizing the effects of baroclinicity in barotropic models the modeler's primary concern is making the layer of interest behave as it would in a baroclinic ocean. For example, when using a barotropic vorticity model, a common practice is to dissipate energy at large scales while inputting energy at smaller scales (e.g., Haidvogel and Keffer, 1984; Babiano et al., 1987). The purpose of this is to override the energy cascade to large scales, thus effectively imposing a dominant length scale which matches oceanic observations. Another method of imposing such a length scale is to explicitly impose a deformation radius, $\sqrt{\lambda}$, e.g.,

$$\left[\frac{\partial}{\partial t} + \frac{\partial \psi}{\partial x}\frac{\partial}{\partial y} - \frac{\partial \psi}{\partial y}\frac{\partial}{\partial x}\right]\left[\nabla^2 \psi - \frac{1}{\lambda}\psi + \beta y\right] = 0, \tag{B.9}$$

(*i.e.*, make it a $1\frac{1}{2}$ layer model) as is done, for example, by Holloway and Kristmannsson (1984). Again, the ultimate purpose of such an approach is to force some of the energy from the barotropic mode to the smaller length scales of the baroclinic modes. There remains, however, an important difference between the barotropic and baroclinic modes in terms of the time scale of the motion. Namely, for identical length scales (or in terms of equation (B.2), identical horizontal wave number) the time scale of the barotropic mode is expected to be smaller than those of the baroclinic modes. This appears to be a factor in my attempts to use a barotropic vorticity model to simulate the flow in the North Atlantic Tracer Release Experiment. Namely, in the barotropic model (see equation (3.1)), when I adjust the kinetic energy level and the dominant length scale through an *ad hoc* forcing and dissipation, the resulting time scale is then somewhat smaller than is seen in the

observations. Thus, although these *ad hoc* forcing and dissipation terms seem to address the differences in length scales associated with the barotropic and baroclinic modes, they do not address the issue of Rossby wave propagation speeds.

In summary, based on the above discussion, it appears that proper calibration of barotropic models in terms of kinetic energy and the dominant length scale may be achieved, however, the relatively long time scales appropriate to baroclinic flow are probably not directly accessible to these models.

Appendix C

The qgb Model – a "technical report"

C.1 Introduction

C.1.1 Background

The "qgb" code is a two layer, semi-spectral, quasi-geostrophic, potential vorticity model which was originally by Bill Dewar and modified significantly by Glenn Flierl. The present documentation was compiled and formatted by Miles Sundermeyer (MAS) based on a collection of personal notes, as well as notes from Joseph Lacasce (JHL) and Audrey Rogerson (AMR). The purpose of these notes is to assist new users with the model. algorithms will be of help. This documentation is intended only as a helpful aid, and does not include descriptions of every detail of the model (some versions of the model have features which are not described here).

This document is organized as follows. In this introduction, a brief background of the model is given, along with a short description of the major features. In section two, I describe the model equations, including the two layer quasi-geostrophic potential vorticity equations and the advective/diffusive equation. The equations are non-dimensionalized, and

the key non-dimensional parameters and their meanings are discussed. Section three gives some details of the numerical implementation including two dimensional discrete Fourier transforms and the time stepping method. Section four outlines the flow of the code, describing the major proceedures and subroutines. Section five includes a description what is needed for compilation, parameter files, and initial conditions. The form of the model output is also described, and list of model variables is given.

C.1.2 Model overview

The basic model is run on a square domain with doubly periodic boundaries. Computations are done in Fourier space, with the exception of the non-linear terms which are computed in real space. One or two layers may be included, along with some number of passive scalar fields and bio-fields. The model can be run on a $\beta-$ or $f-$plane, and may accommodate a mean flow as well as a linearly sloping bottom. The code is written in modular form, with the operating parameters (such as how many layers and how many scalar fields) being set before compilation in order to minimize computation. Other parameters such as time step, grid spacing, etc., and initial conditions are read in from separate files so as to not require re-compilation. The code does not require any external library function calls (for example, it includes its own two dimensional fft algorithm), and should be platform independent.

C.2 Model Formulation

The model can be viewed as being either non-dimensional or dimensional, as the user prefers. However, since the non-dimensional view lends itself to a much broader interpretation, this is what is developed here. In this section, I review the dimensionful PV equations for the two layer system. The equations are then non-dimensionalized and the meanings of the relevant non-dimensional parameters are discussed.

C.2.1 The Potential Vorticity Equation

Dimensionful

The quasi-geostrophic potential vorticity equations for a two-layer system can be expressed as,

$$\left[\frac{\partial}{\partial t} + \frac{\partial \psi_1}{\partial x}\frac{\partial}{\partial y} - \frac{\partial \psi_1}{\partial y}\frac{\partial}{\partial x}\right]\left[\nabla^2\psi_1 - F_1(\psi_1 - \psi_2) + \beta y\right] = \nabla^4\psi_1, \qquad (C.1)$$

$$\left[\frac{\partial}{\partial t} + \frac{\partial \psi_2}{\partial x}\frac{\partial}{\partial y} - \frac{\partial \psi_2}{\partial y}\frac{\partial}{\partial x}\right]\left[\nabla^2\psi_2 - F_2(\psi_2 - \psi_1) + \beta y + h(y)\right] = \nabla^4\psi_2 - \frac{r}{2}\nabla^2\psi_2, \quad (C.2)$$

(e.g., Pedlosky, 1987) where β is the meridional gradient of the Coriolis parameter, $h(y)$ is bottom topography, $\nabla^2 = \frac{\partial^2}{\partial x^2} + \frac{\partial^2}{\partial y^2}$, ψ_i is the geostrophic stream function in i^{th} layer, $i = 1, 2$, which satisfies

$$(u_i, v_i) = \hat{k} \times \nabla\psi_i = \left(\frac{-\partial \psi_i}{\partial y}, \frac{\partial \psi_i}{\partial x}\right), \qquad (C.3)$$

and F_i is the inverse deformation radius squared for i^{th} layer,

$$F_i = \frac{f^2}{g'D_i}, \qquad (C.4)$$

$g' = g\frac{\Delta\rho}{\rho}$ is reduced gravity and f is the Coriolis parameter. The above two equations may be expressed in compact form as

$$\left[\frac{\partial}{\partial t} + \frac{\partial \psi_i}{\partial x}\frac{\partial}{\partial y} - \frac{\partial \psi_i}{\partial y}\frac{\partial}{\partial x}\right]\left[\nabla^2\psi_i - F_i(\psi_i - \psi_j)\right] + \beta_i\frac{\partial \psi_i}{\partial x}$$
$$= \mu_{1i}\nabla^{2(n_1+1)}\psi_i + \mu_{2i}\nabla^{2(n_2+1)}\psi_i.$$

with the quasi-geostrophic potential vorticity for each layer given by

$$q_i = \nabla^2\psi_i - F_i(\psi_i - \psi_j) + f_o + \beta_i, \qquad (j = 3 - i). \qquad (C.5)$$

The potential vorticity in the ith layer is composed of a relative vorticity $\nabla^2\psi_i = v_{ix} - u_{iy}$, and a stretching term, $F_i(\psi_j - \psi_i)$. The latter is due to the motion of the interface, and is the simplest way to introduce the effects of stratification. The planetary vorticity gradient is accounted for in the beta term, which may also include effects of bottom topography and/or a mean flow (hence β_i represents effective β, which may be different in the two layers; see below).

Bottom topography

73

In the above formulation, the β term represents the overall mean potential vorticity gradient. This can be due to a change in the Coriolis parameter with latitude (the β-plane approximation), and/or for the lower layer or the barotropic case due to, say, a linearly sloping bottom, $H(y)$. The effect of such bottom topography is most easily seen by considering the barotropic potential vorticity,

$$q = \frac{\nabla^2 \psi + f_o + \beta y}{H(y)}, \tag{C.6}$$

where $H(y) = H_o - h(y)$ and $|h(y)| \ll |H_o|$. Using a binomial expansion on $H(y)$,

$$q \approx \frac{\nabla^2 \psi + f_o + \beta y}{H_o} \left(1 + \frac{h(y)}{Ho}\right). \tag{C.7}$$

Noting that the quasi-geostrophic formulation assumes small Rossby number, $R_o = U/fL$, i.e., $\nabla^2 \psi \ll f_o$, and that $\beta y \ll f_o$, terms where either of these multiply $h(y)/H_o$ can be neglected, it follows that

$$q \approx \frac{1}{H_o} \left(\nabla^2 \psi + f_o + \beta y + \frac{f_o h(y)}{H_o}\right), \tag{C.8}$$

which says that for a linear bottom slope, $h(y)$, the effect of topography is equivalent to that of planetary β. It is useful to keep in mind that the above "topographic beta" formulation only applies if changes in the layer depth are small compared to the total depth. In addition, both advection and the planetary vorticity gradient must be small compared to f_o for the neglect of higher order terms to be valid. As noted below, this idealized from of bottom topography, a linear slope in y, is the only form presently allowed in the model, however, this may easily be changed.

Background Flow

The quasi-geostrophic potential vorticity equation can also be made to incorporate a simple zonal shear flow by replacing ψ_i with $(-\overline{u_i}y + \psi_i)$. The PV equation then becomes, in long form,

$$\left[\frac{\partial}{\partial t} + \frac{\partial \psi_i}{\partial x}\frac{\partial}{\partial y} - \frac{\partial \psi_i}{\partial y}\frac{\partial}{\partial x} + \overline{u_i}\frac{\partial}{\partial x}\right] \left[\nabla^2 \psi_i - F_i(\psi_i - \psi_j)\right] + \beta\frac{\partial \psi_i}{\partial x} + (\overline{u_i} - \overline{u_j})F_i\frac{\partial \psi_i}{\partial x}$$
$$= \mu_{1i}\nabla^{2(n_1+1)}\psi_i + \mu_{2i}\nabla^{2(n_2+1)}\psi_i.$$

Letting β_i' be the augmented potential vorticity gradient in i^{th} layer,

$$\beta_i' = \beta_i + (\overline{u_i} - \overline{u_j})F_i,$$

this can be re-written as

$$\left[\frac{\partial}{\partial t} + \frac{\partial \psi_i}{\partial x}\frac{\partial}{\partial y} - \frac{\partial \psi_i}{\partial y}\frac{\partial}{\partial x} + \overline{u_i}\frac{\partial}{\partial x}\right]\left[\nabla^2 \psi_i - F_i(\psi_i - \psi_j)\right] + \beta_i'\frac{\partial \psi_i}{\partial x}$$
$$= \mu_{1i}\nabla^{2(n_1+1)}\psi_i + \mu_{2i}\nabla^{2(n_2+1)}\psi_i.$$

There are thus two contributions of a mean zonal shear flow to the potential vorticity balance in each layer. The first is the advection of the potential vorticity due to the mean flow $(\overline{u_i}\partial q_i/\partial x)$. The second is the contribution to vortex stretching due to the change in layer thickness, $((\overline{u_i} - \overline{u_j})F_i\partial \psi_i/\partial x)$, required by geostrophy to maintain the pressure gradient driving the flow. From the perspective of the top layer, the effect of the interface slope are similar to that of a sloping bottom, i.e., the bottom slope may be thought of in terms of an effective beta, $\beta_{interface} = fh_y/H_1$, where h_y is given by the thermal wind relation, $fu_z = g\rho_y/\rho_o$. This change in layer thickness may be due, in the barotropic case, to a change in the free surface elevation, or in the two layer system, to interface displacements.

Non-dimensional

In light of the above discussions, without loss of generality, the simple case of no bottom slope and no mean flow will be considered. The potential vorticity equation may be expressed as

$$
\overset{\text{(a)}}{} \quad \overset{\text{(b)}}{} \quad \overset{\text{(c)}}{} \quad \overset{\text{(d)}}{} \quad \overset{\text{(e)}}{} \quad \overset{\text{(f)}}{}
$$
$$\frac{\partial}{\partial t}\nabla^2 \psi_i - \frac{\partial}{\partial t}F_i(\psi_i - \psi_j) + J(\psi_i, \nabla^2 \psi_i - F_i(\psi_i - \psi_j)) + \beta_i\frac{\partial \psi_i}{\partial x} = \mu_i\nabla^{2(n+1)}\psi_i. \qquad \text{(C.9)}$$

Assuming a length scale, L, and a velocity scale, U, an advective time scale may be defined, $T = U/L$. With

$$[x, y, t, \psi_i] \sim [Lx^*, Ly^*, \frac{L}{U}t^*, LU\psi_i^*], \qquad \text{(C.10)}$$

the relative vorticity scales as

$$\nabla^2 \psi_i \sim \frac{U}{L}\psi_i^*. \qquad \text{(C.11)}$$

Non-dimensionalizing equation (C.9) (remembering that the Jacobian operator carries two derivatives, hence a $1/L^2$), individual terms scale as

$$
\overset{\text{(a)}}{} \quad \overset{\text{(b)}}{} \quad \overset{\text{(c)}}{} \quad \overset{\text{(d)}}{} \quad \overset{\text{(e)}}{} \quad \overset{\text{(f)}}{}
$$
$$\left(\frac{U^2}{L^2}\right) \quad \left(U^2 F_i\right) \quad \left(\frac{U^2}{L^2}\right) \quad \left(U^2 F_i\right) \quad (U\beta) \quad \left(\frac{\mu_{n_i}}{L^{2n}}\frac{U}{L}\right). \qquad \text{(C.12)}$$

Multiplying through by (L^2/U^2),

<div align="center">

(a)   (b)   (c)   (d)   (e)   (f)

</div>

$$ (1) \quad (L^2 F_i) \quad (1) \quad (L^2 F_i) \quad \left(\frac{L^2}{U}\beta\right) \quad \left(\frac{\mu_{n_i}}{U L^{2n-1}}\right), \tag{C.13} $$

which then gives the three relevant non-dimensional parameters for the PV equation in each layer: $\hat{F}_i$ in the nondimensional Froude number for i^{th} layer, $\hat{\beta}_i$ is nondimensional beta in i^{th} layer and $\hat{\mu}_{n_i}$ is the inverse of the Reynolds number:

$$ \left. \begin{aligned} \hat{F}_i &= L^2 F_i = \frac{L^2}{L_{R_i}^2} \\ \hat{\beta}_i &= \frac{L^2}{U}\beta_i = \frac{L^2}{L_{\beta_i}^2} \\ \hat{\mu}_{n_i} &= \frac{\mu_{n_i}}{U L^{2n-1}} = \frac{L}{L_{\mu_{n_i}}}. \end{aligned} \right\} \tag{C.14} $$

Using the above parameters, the non-dimensional PV equation can be expressed as

$$ \frac{\partial}{\partial t^*}\nabla^2\psi_i^* - \frac{\partial}{\partial t^*}\hat{F}_i(\psi_j^* - \psi_i^*) + J(\psi_i^*, \nabla^2\psi_i^* + \hat{F}_i(\psi_j^* - \psi_i^*)) + \hat{\beta}_i\frac{\partial\psi_i^*}{\partial x^*} = \hat{\mu}\nabla^{2(n+1)}\psi_i^*. \tag{C.15} $$

In terms of the non-dimensional parameters derived above, the relative importance of vortex stretching in the total vorticity balance is determined by $\hat{F}$, which measures the ratio of the scale of motion, L, to the deformation radius, $\sqrt{g'H}/f$. Small $\hat{F}$ implies that on the scale of the motion, contributions to the potential vorticity by vortex stretching due to variations of the interface are negligible, $i.e.$, the interface is very rigid. In this case, the motion in the two layers is uncoupled. Conversely, large $\hat{F}$ implies that on the scale of the motion, vortex stretching dominates over the relative vorticity, and the layers interact more strongly. On these scales motion in the two layers is similar and the fluid tends to behave barotropically ($e.g.$, Pedlosky, 1979).

The relative importance of planetary vorticity gradients (or vorticity gradients due to a sloping bottom or mean flow as discussed above) are determined by $\hat{\beta}$. This term represents the importance of linear Rossby waves compared to advection (or eddies). Thought of in terms of a ratio of length scales (see equation (C.14)), if the scale of motion, L, is small compared to the "arrest" scale, L_{β_i}, then the fluid does not feel the PV gradient, and advection dominates. On the other hand, if L is large compared to L_{β_i} then the flow is dominated by wave motions.

As expressed in equation (C.15), the dissipation terms in the model takes the form

$$ D = \mu\nabla^{2(n+1)}\psi_i^*, $$

<div align="center">

76

</div>

which, for appropriate choices of μ and n may represent linear bottom friction, lateral mixing, or higher order ("scale selective") diffusion terms. (Note that n_1 and n_2 are the *order of the Laplacian in the momentum equations*, e.g., bottom friction $\Rightarrow n = 0$, Newtonian viscosity $\Rightarrow n = 1$, super viscosity $\Rightarrow n = 2$, etc. This will be brought to light again in the discussion of the model implementation.) Again thinking in terms of a ratio of length scales as expressed in equation (C.14), the relative importance of the dissipation terms is clear.

To summarize, the relevant non-dimensional parameters in the potential vorticity equation (C.15) are most easily interpreted as a ratio of length scales (see equation (C.14)). As an example, suppose the deformation radius was $L_R \approx 40\ km$, the β arrest scale was $L_\beta \approx 150\ km$, and the damping scale was $L_{\nu_n} \approx 10^{-1}\ km$. This would then mean that the largest scales are dominated by planetary vorticity gradients, the smallest scales by dissipation, and intermediate scales by baroclinic interactions (surface displacements for the single layer case).

C.2.2   The Advective/Diffusive Equation

Given a flow field specified by $\psi(x, y, t)$ as above, the distribution of a passive tracer, θ, may be computed using the advective/diffusive equation,

$$\frac{D}{Dt}\theta = \frac{\partial \theta}{\partial t} + J(\psi, \theta) = \eta \nabla^2 \theta, \tag{C.16}$$

where η is the coefficient of lateral diffusion. Expressing the right hand side in a manner similar to the PV equation, this becomes

$$\frac{D}{Dt}\theta = \frac{\partial \theta}{\partial t} + J(\psi, \theta) = \eta \nabla^{2(n+1)}\theta, \tag{C.17}$$

where $n = 0$ would correspond to a Fickian diffusion. Using the same scales as above (equation (C.14)), the non-dimensional advective/diffusive equation can be characterized by a single parameter, the sub-gridscale diffusivity

$$\hat{\eta} = \frac{\eta}{U L^{2n-1}} = \frac{L}{L_\eta}. \tag{C.18}$$

In non-dimensional form, the advective/diffusive equation is

$$\frac{D}{Dt^*}\theta^* = \frac{\partial \theta^*}{\partial t^*} + J(\psi^*, \theta^*) = \hat{\eta} \nabla^{2(n+1)}\theta^*. \tag{C.19}$$

77

C.3 Numerical Implementation

C.3.1 Model Equations, Parameters

Equations (C.15) and (C.19) make up the main engine of the qgb model. For completeness, the non-dimensional potential vorticity equation with a mean flow is given by

$$\left[\frac{\partial}{\partial t} + \frac{\partial \psi_i}{\partial x} \frac{\partial}{\partial y} - \frac{\partial \psi_i}{\partial y} \frac{\partial}{\partial x} + \overline{u_i} \frac{\partial}{\partial x} \right] \left[\nabla^2 \psi_i - \hat{F}_i (\psi_i - \psi_j) \right] + \hat{\beta}_i' \frac{\partial \psi_i}{\partial x}$$
$$= \hat{\mu}_{1i} \nabla^{2(n_1+1)} \psi_i + \hat{\mu}_{2i} \nabla^{2(n_2+1)} \psi_i.$$

where the *'s have been omitted and all quantities are assumed non-dimensional.

The meaning of non-dimensional parameters, $\hat{F}$, $\hat{\beta}$, and $\hat{\mu}$ has been discussed in the previous section. In practice, the qgb model actually uses two parameters, the inverse baroclinic deformation radius, γ, defined by

$$\gamma^2 \equiv \hat{F}_1 + \hat{F}_2 = \frac{f^2 L^2}{g'} \left(\frac{1}{D_1} + \frac{1}{D_2} \right) \tag{C.20}$$

and the ratio of the upper layer depth to the lower layer depth δ,

$$\delta \equiv \frac{D_1}{D_2} \tag{C.21}$$

to determine $\hat{F}_i$. The non-dimensional Froude numbers for each layer are recovered by

$$\hat{F}_1 = \frac{\gamma^2}{1 + \delta}, \qquad \hat{F}_2 = \frac{\delta \gamma^2}{1 + \delta}. \tag{C.22}$$

The qgb model assumes that β_i is aligned so that the potential vorticity gradient is in the y direction. As such, the model can presently incorporate a zonal shear flow and bottom topography which is a linear function of y. However, with a few simple changes to the code, potential vorticity gradients in the east-west direction are easily included in the model. (Contributions to effective β_i due to the shear flow are made in qgb.F immediately after the parameters are loaded in, while advective effects are included in the qgbjac.F subroutine. Topographic β in the lower layer is specified as an input parameter as part of the appropriate (effective) β term.

C.3.2   The Solution Technique

By assumption, ψ_i and θ are periodic in each horizontal direction, and the governing equations may be represented by a double Fourier series. A pseudo-spectral technique is then used to integrate forward in time. In this scheme, all computation is done in Fourier space, with the exception of the nonlinear terms, for which multiplication is done in real space. Leapfrog time-differencing is used to advance the potential vorticity and tracer fields, with an Euler step applied every 50 time steps to avoid divergence of solutions. Dissipation is handled semi-implicitly in order to avoid unconditional computational instability.

The Fourier projection of the geostrophic stream function, ψ_i can be expressed as

$$\psi_i = \Re e(\hat{\psi}_i e^{ikx} e^{ily}), \tag{C.23}$$

where $\Re e$ denotes the real part. From now on this symbol will be dropped. The relative vorticity field in Fourier space is then given by

$$\widehat{\nabla^2 \psi_i} = -(k^2 + l^2)\hat{\psi}_i = -K^2 \hat{\psi}_i \tag{C.24}$$

and the potential vorticity field by

$$\hat{q}_i = -(K^2 + F_i)\hat{\psi}_i + F_i \widehat{\psi_{3-i}}, \tag{C.25}$$

where $K \equiv \sqrt{k^2 + l^2}$ is the total horizontal wavenumber. In the above, it is seen that spatial derivatives can be computed in Fourier space by multiplying the transformed quantity by the appropriate wave vector component. For example, the Fourier transform of $\partial \psi / \partial x$ is computed as

$$\left(\widehat{\frac{\partial \psi}{\partial x}} \right) = -ik\hat{\psi}. \tag{C.26}$$

To compute the non-linear Jacobian terms, the qgb code transforms the potential vorticity and velocity back into real space in order to perform multiplication. In the interest of numerical efficiency, this is done instead of taking the convolution in Fourier space (in two dimensions, it can be shown that the convolution requires on the order of $(N^2)^2$ operations, while the "semi-spectral" technique only requires $N^2 \log_2 N^2$ operations). One of the difficulties that arises from this short-cut is that it introduces contributions from unresolved small scales ($K > K_{max}$) during the forward and inverse Fourier transformations. To combat such aliasing, a truncation matrix, *trunc*, is introduced in the qgb code to partially filter these contributions. For a more thorough treatment of the aliasing problem, methods

79

such as those outlined by Orszag (1971) may be implemented, however, experimentation by JHL with such de-aliasing techniques suggests that the effects of truncation are not large, and in the interest of numerical efficiency, the present use of *trunc* suffices. For those who wish to improve over the *trunc* matrix without the additional computational costs, a simple method of applying a filter in Fourier space can been exploited. AMR, for example, has had success in alias reduction by replacing the *trunc* matrix with a smoother filter.

C.3.3 Time Stepping / Implicit Treatment of Forcing

The numerical time stepping is most easily understood by thinking of the potential vorticity equation in a vector form as:

$$\frac{\partial \hat{q}}{\partial t} = -\mathbf{J} + \mathbf{D}\hat{\psi}, \tag{C.27}$$

where $\hat{q} = (q_1, q_2)^T$ is now a potential vorticity column vector and $\hat{\psi} = (\psi_1, \psi_2)^T$ is a streamfunction column vector, $\mathbf{J}$ is a column vector representing the Jacobian terms, and matrix $\mathbf{D}$ represents the friction terms in Fourier space and is given by

$$\mathbf{D} = \begin{bmatrix} \hat{\mu}_{11}(-K^2)^{n_1+1} + \hat{\mu}_{21}(-K^2)^{n_2+1} & 0 \\ 0 & \hat{\mu}_{12}(-K^2)^{n_1+1} + \hat{\mu}_{22}(-K^2)^{n_2+1} \end{bmatrix}. \tag{C.28}$$

The leapfrog scheme is used to step the Fourier coefficients of $\hat{\psi}$ forward in time,

$$\hat{q}^{n+1} - \Delta t \mathbf{D}\hat{\psi}^{n+1} = \hat{q}^{n-1} + \Delta t \mathbf{D}\hat{\psi}^{n-1} - 2\Delta t \mathbf{J}^n, \tag{C.29}$$

where the superscript denotes the discrete time. The relationship between $\hat{q}$ and $\hat{\psi}$ as given in equation (C.25) can be expressed in a matrix operator form as

$$\hat{q} = -\mathbf{A}\hat{\psi}, \qquad \mathbf{A} = \begin{bmatrix} K^2 + F_1 & -F_1 \\ -F_2 & K^2 + F_2 \end{bmatrix}. \tag{C.30}$$

The finite difference equation (C.29) can be expressed as

$$(-\mathbf{A} - \Delta t \mathbf{D})\hat{\psi}^{n+1} = (-\mathbf{A} + \Delta t \mathbf{D})\hat{\psi}^{n-1} - 2\Delta t \mathbf{J}^n. \tag{C.31}$$

Re-arranging terms, the leap-frog time evolution equation may be expressed in terms of single left and right hand side matrix operators acting on a column vector $\hat{\psi} = (\psi_1, \psi_2)^T$,

$$\underbrace{\left(\frac{\mathbf{A}}{2\Delta t} + \frac{\mathbf{D}}{2}\right)}_{\mathbf{A}_{left}} \hat{\psi}^{n+1} = \underbrace{\left(\frac{\mathbf{A}}{2\Delta t} - \frac{\mathbf{D}}{2}\right)}_{\mathbf{A}_{right}} \hat{\psi}^{n-1} + \mathbf{J}^n. \tag{C.32}$$

80

In full, these left and right hand side operators are:

$$\mathbf{A}_{left} = \begin{bmatrix} \frac{K^2+F_1}{2\Delta t} + \frac{\mathbf{D}_{11}}{2} & \frac{-F_1}{2\Delta t} \\ \frac{-F_2}{2\Delta t} & \frac{K^2+F_2}{2\Delta t} + \frac{\mathbf{D}_{22}}{2} \end{bmatrix}$$

$$= \begin{bmatrix} K^2\left(\frac{1}{2\Delta t} + \text{FRC}\right) + \frac{F_1}{2\Delta t} & \frac{-F_1}{2\Delta t} \\ \frac{-F_2}{2\Delta t} & K^2\left(\frac{1}{2\Delta t} + \text{FRC}\right) + \frac{F_2}{2\Delta t} \end{bmatrix}, \qquad \text{(C.33)}$$

$$\mathbf{A}_{right} = \begin{bmatrix} \frac{K^2+F_1}{2\Delta t} - \frac{\mathbf{D}_{11}}{2} & \frac{-F_1}{2\Delta t} \\ \frac{-F_2}{2\Delta t} & \frac{K^2+F_2}{2\Delta t} - \frac{\mathbf{D}_{22}}{2} \end{bmatrix}$$

$$= \begin{bmatrix} K^2\left(\frac{1}{2\Delta t} - \text{FRC}\right) + \frac{F_1}{2\Delta t} & \frac{-F_1}{2\Delta t} \\ \frac{-F_2}{2\Delta t} & K^2\left(\frac{1}{2\Delta t} - \text{FRC}\right) + \frac{F_2}{2\Delta t} \end{bmatrix}, \qquad \text{(C.34)}$$

where $\mathbf{D}_{ii}/2 \equiv K^2(\text{FRC})$, and FRC represents the friction operator explicitly used in the qgb code.

Using the leap-frog time stepping as described above, two independent progressions in time occur,

$$(n = 1 \rightarrow 3 \rightarrow 5 \rightarrow 7 \ldots)$$
$$(n = 2 \rightarrow 4 \rightarrow 6 \rightarrow 8 \ldots). \qquad \text{(C.35)}$$

As a result, random contributions due to numerical error will cause these solutions to diverge in an un-physical manner. To inhibit this tendency, an Euler time step is used to "re-unite" solutions every 50th time step,

$$\hat{q}^{n+1} = \hat{q}^n + \Delta t(-\mathbf{J}^n + \mathbf{D}\hat{\psi}^n). \qquad \text{(C.36)}$$

The finite difference equation for the Euler time steps becomes

$$\hat{q}^{n+1} - \frac{\Delta t}{2}\mathbf{D}\hat{\psi}^{n+1} = \hat{q}^n + \frac{\Delta t}{2}\mathbf{D}\hat{\psi}^n - \Delta t\mathbf{J}^n, \qquad \text{(C.37)}$$

Similar to above, this may be written as

$$\underbrace{\left(\frac{\mathbf{A}}{\Delta t} + \frac{\mathbf{D}}{2}\right)}_{\mathbf{A}_{left}}\hat{\psi}^{n+1} = \underbrace{\left(\frac{\mathbf{A}}{\Delta t} - \frac{\mathbf{D}}{2}\right)}_{\mathbf{A}_{right}}\hat{\psi}^n + \mathbf{J}^n, \qquad \text{(C.38)}$$

where the left and right hand side operators are based on Δt instead of $2\Delta t$ as for the leap-frog.

C.3.4 Dissipation Terms

As mentioned above, the dissipation terms in the model are expressed in the form

$$\mu_i \nabla^{2(n+1)} \psi_i, \tag{C.39}$$

where n represents the order of the Laplacian in the momentum equations. Hence,

Bottom friction:

$$-\lambda(\nabla \times \vec{u}) = -\lambda \nabla^2 \psi \qquad\qquad n = 0, \quad \mu = -\lambda < 0$$

Newtonian viscosity:

$$\nu \nabla^2(\nabla \times \vec{u}) = \nu \nabla^2(\nabla^2 \psi) \qquad\qquad n = 1, \quad \mu = \nu > 0$$

Super viscosity:

$$\nu_4 \nabla^4(\nabla \times \vec{u}) = -\nu_4 \nabla^4(\nabla^2 \psi) \qquad\qquad n = 2, \quad \mu = -\nu_4 < 0$$

...etc.

From here, it is clear that the dissipation term can be written in Fourier space as

$$
\begin{aligned}
\mathcal{F}(\mu \nabla^{2(n+1)} \psi) &= \mu(-K^2)^{n+1} \hat{\psi} \\
&= \mu(-1)^{n+1} K^{2n}(K^2 \hat{\psi}) \\
&= \begin{cases} -\mu K^{2n}(K^2 \hat{\psi}) & n \text{ even} \\ +\mu K^{2n}(K^2 \hat{\psi}) & n \text{ odd} \end{cases} \\
&= |\mu| K^{2n}(K^2 \hat{\psi}) \\
&= \mathbf{D}\hat{\psi}
\end{aligned}
$$

where $\mathbf{D}$ is the same dissipation operator described in the time stepping. Letting

$$\frac{\mathbf{D}_{ii}}{2} = K^2 \text{ FRC}, \qquad \text{FRC} = \frac{1}{2}|\mu| K^{2n}, \tag{C.40}$$

this dissipation operator can be expressed in terms of the variable FRC, as is done in the qgb code (see qgbinit.F). Note that although different order dissipation terms are of different signs as above, for the nth order dissipation, it is the absolute value, $|\mu_n|$, which must be specified in the qgb code.

C.3.5 Discretization and 2-d FFT's

To implement the above equations, the model domain is represented by a grid of $(nx \times ny)$ evenly spaced points, where nx, and ny must be powers of 2 (typically, $N = nx = ny$, and in fact through the many different generations of the qgb code, it appears this has been assumed. The user wishing to have a non-square grid is therefore cautioned to check the code for instances where nx and ny are used interchangeably under the assumption that they are equal.) The continuous, two-dimensional Fourier transform, defined as

$$\mathcal{F}(h(x,y)) = \tilde{h}(k,l) = \int_{-\infty}^{\infty} \int_{-\infty}^{\infty} h(x,y) e^{2\pi i (kx + ly)} dx dy \tag{C.41}$$

is represented by the discrete Fourier series

$$\mathcal{F}(h(x,y)) = \tilde{h}(k,l) = \frac{1}{nx} \frac{1}{ny} \sum_{k=-\frac{nx}{2}}^{\frac{nx}{2}-1} \sum_{l=-\frac{ny}{2}}^{\frac{ny}{2}-1} h(x,y) e^{2\pi i (kx + ly)}, \tag{C.42}$$

where the series has been truncated at the cutoff wavenumber in each direction. In order to improve efficiency in doing the above summations, the model makes use of one of the symmetries of the Fourier series. For a real function, $h(x)$, the Fourier transform $\tilde{h}(k)$ has the property

$$\tilde{h}(-k) = \left[\tilde{h}(k)\right]^*, \tag{C.43}$$

where '*' represents the complex conjugate. This means that the matrix representing the two-dimensional discrete Fourier transform $\tilde{h}(k,l)$ has the form (schematically)

$$\tilde{h}(k,l) = \begin{pmatrix} 1,1 & (a) & 1,nc & (\overleftrightarrow{a^*}) \\ (b) & \boxed{f} & (d) & \boxed{g} \\ nc,1 & (e) & nc,nc & (\overleftrightarrow{e^*}) \\ \updownarrow(b^*) & \updownarrow\boxed{\overleftrightarrow{g^*}} & \updownarrow(d^*) & \updownarrow\boxed{\overleftrightarrow{f^*}} \end{pmatrix}, \tag{C.44}$$

where $nc = \left(\frac{nx}{2} + 1\right)$, the ()'ed variables represent one-dimensional arrays of length nc, the $\Box$'ed variables represent submatrices of size $\left(\frac{nx}{2} - 1\right) \times \left(\frac{nx}{2} - 1\right)$, and $\longleftrightarrow$ and $\updownarrow$ indicate horizontal and vertical "flipping", respectively, of the sub-arrays. Utilizing this symmetry, the qgb model only keeps track of $(nc \times ny)$ instead of $(nx \times nx)$ elements in Fourier space.

C.4 Model Flow

The **qgb** main program begins by including **qgbcom.f**, which contains the "common block" parameter and variable declarations. It then reads in the "post compilation"

parameters from the designated input file. For the two layer system with a mean flow, $\overline{u_i}$, effective β is computed to account for the interface slope. Next, (*ncomp*) records, representing [ψ_i, h, *passive scalars*, *bio fields*] are read in from the initial conditions file. The code then calls **qgbinit**, where it defines the wave number matrix K^2, the Fourier space version of the friction operators, FRC, and the truncation matrix, *trunc*. The initial conditions are transformed into Fourier space, and the friction and time dependent terms in the governing equations are evaluated in order to prepare for the first time step.

Flow returns to **qgb**, where **qgstep** is then called to perform the time integration. Within **qgstep**, the program first calls **qgjac** in order to compute the Jacobian terms. In **qgbjac**, the Fourier transformed potential vorticities for the two layers are computed. PV and all scalars are truncated, and transformed back into real space for later use. Next, the $\left(\beta \frac{\partial \psi}{\partial x}\right)$ term is computed in Fourier space. The meridional advection term, $\frac{\partial}{\partial y}(vq)$ is then computed by multiplying velocity and PV in real space, and then transforming back to Fourier space to perform differentiation. Finally, the zonal advection term $\frac{\partial}{\partial x}((u + \overline{u})q)$, is computed by transforming u to real space, adding $\overline{u}$, multiplying the sum by q, and again transforming back to Fourier space to perform differentiation. The Jacobian terms for each field are added as rhs terms in their respective equations, and the program then returns to **qgstep**.

Back in **qgstep**, the program is about ready to time step the potential vorticity and advective / diffusive equations. As described in the previous sections, these can collectively be thought of in the general form

$$\frac{\partial}{\partial t}(\bullet) = -\mathbf{J}(\psi_i, \bullet) - \mathbf{D} \cdot (\bullet), \tag{C.45}$$

(see equation (C.27)) where ($\bullet$) represents the various fields, *i.e.*,

$$\bullet = \begin{cases} \hat{q}_i & \text{for layer 1 \& 2 PV} \\ \hat{h} & \text{for interface height} \\ \widehat{(scalar)}_i & \text{for passive scalars} \\ \widehat{(bio)}_i & \text{for bio fields} \end{cases} \tag{C.46}$$

and the Jacobian is that appropriate for the particular field being stepped. That is, the β term in the Jacobian is only included when operating on the potential vorticity, not on passive scalars (actually, in some versions of the code, large-scale gradients for scalar fields may also be specified). Since all the terms on the rhs of equation (C.29) have been computed, the program is now ready to step forward in time. Back in **qgstep**, the program

84

decides which kind of time step is required for the current iteration, according to the current value of *NSTEP*. The operators $\mathbf{A}_{left}$ and $\mathbf{A}_{right}$ are computed (see equations (C.33) and C.34) and the new $\hat{\psi}_i$ (and scalar fields) are computed according to the appropriate finite difference equation (*i.e.*, according to which field and whether it is time to do a leap-frog or an Euler time step). As appropriate, vertical velocity, and scalar fields, are also stepped forward in time, biological corrections are applied, and h is diagnosed. The code then checks if it is time to dump to disk, and does so if appropriate. Having completed the present time step, the code returns to the beginning of **qgbstep** to begin next time step with a call to **qgbjac**. The code cycles through **qgbstep**, applying leap-frog time stepping with an Euler step every 50th step until the specified number of iterations has been completed.

C.5 Hands On ...

C.5.1 Files

Relevant files to the code are:

- Set-up / initial condition files
  - Makefile
  - Initial conditions (see below)
  - param (*parameters file*)

- Main QGB code and subroutines
  - qgb.F
  - qgbcom.f
  - qgbinit.F
  - qgbstep.F
  - qgfftma.f
  - qgbjac.F
  - qgbbio.f
  - qgbcalh.F

Note, this is not a complete list of files available for the qgb code. These are only the "core" files. For example, this list does not include all of the files necessary for bio fields and vertical velocity, nor does it include numerous subroutines for float tracking and forcing such as those developed by MAS, JHL, and AMR.

C.5.2 Running the Model: Set-Up / Initial Conditions

qgbcom.f

Before compiling, the parameters in the file **qgbcom.f** file must be modified to suit the users particular application. A description of these parameters is given below, along with example values appropriate for a single layer with one passive scalar field and no bio fields:

(nx=128,ny=128) – Sets the grid size to be 128 × 128.

(ncomp=2,npsi=1) – Sets the total number of fields (ncomp = ψ + h + scalars + bio), and the number of ψ fields.

(nscalar=1) – Sets the number of the first scalar field (includes bio fields).

(nbio=0,nnbio=0) – Sets the number of the first bio field, and the total number of bio fields.

c#define DOH – Comments out blocks which calculate layer thickness.

c#define DOW – Comments out blocks which calculate vertical velocity (incidentally, DOW requires DOH).

#define STEPSCALARS – Defines the scalar time-stepping subroutine.

c#define DOBIO – Comments out biological corrections.

c#define TWOLAYER – Comments out the definition of the two layer subroutines.

Once this file has been edited for the proper configuration, the program is ready for compilation. This is done using the **Makefile** by simply typing "make" at the system prompt.

Initial Conditions

Next, a file containing the initial conditions for the stream function and all scalar variables must be created. All fields must be initialized, with their matrices in the proper sequence within the file. The record ordering is: ψ_1, ψ_2, h, *passive scalars, bio fields*. All fields except for ψ_1 are optional. For example, the parameter settings given above require the binary initial conditions file to contain ψ_1, then *scalar*1 (see the write-up on the initial conditions files for details of how to do this). Remember also that the initial conditions must have the same grid dimensions as was set in **qgbcom.f**.

Parameters

Finally, before running the code, the parameters in the **par.qgb** file must be set. In the basic code, this file consists of six lines, each setting one or more parameter values. Example settings for a single layer with no mean flow are given below, followed by a description of the parameters on each line.

```
4.9062, 4.9062
0.0125, 2000, 200
0.0, 0.0, 0.0, 0.0, 0.0, 0.0
0.1, 0.0, 0.001 ,1.0
0.0
```

where each line represents the parameters

dx,dy – the zonal, and meridional model grid length scale (assumed equal)

dt,ntot,nint – the size of the time step, the total number of time steps to run the model, and the number of time steps between dumps to the output file.

γ^2, δ, β_1, β_2, u_{b_1}, u_{b_2} – the Froude number: $\gamma^2 = \frac{f^2 L^2}{g'}\left(\frac{1}{H_1} + \frac{1}{H_2}\right)$, the aspect ratio $\frac{H_1}{H_2}$, β in layer one, β in layer two , the background velocities in layers one and two

μ_1, n_1, μ_2, n_2 – the coefficient of the first diffusion term, the order of the first diffusion term, the coefficient of the second diffusion term, the order of the second diffusion term

f_0 – the constant part of the Coriolis parameter (used in the Froude#)

Some final things to be noted about the above parameters are as follows:

- A choice of dx = dy = $\frac{2\pi}{nx}$ leads to integer wavenumbers, which tidy up matters of human interpretation of model output and other calculations.

- β_1 and β_2 are not necessarily equal if there is bottom topography (effective beta due to an interface slope is added in automatically).

- u_{b_1}, u_{b_2} are used to compute the interface slope and adjust the effective beta in each layer. They are also used in the advection term to calculate the Jacobian.

The QGB model is executed by typing "qgb ⟨*param-filename*⟩ ⟨*init-cond-filename*⟩" at the system prompt. The code is non-interactive, and the output is dumped to a file whose name is the concatenation of the parameter file name and the initial condition file name. For example, "qgb qgb.param qgb.initcond" will dump its output to the file "qgb.paramqgb.initcond".

References

Babiano, A., C. Basdevant, B. Legras, and R. Sadourny, 1987. Vorticity and passive-scalar dynamics in two-dimensional turbulence. *J. Fluid Mech.*, **183**, 379–397.

Brink, N. J., K. A. Moyer, R. P. Trask, and R. A. Weller, 1993. UOP Technical Report 94-6. The Subduction Experiment. Mooring field program and data summary. Technical report, Woods Hole Oceanographic Inst.

Davis, R. E., 1983. Oceanic property transport, Lagrangian particle statistics, and their prediction. *J. Mar. Res.*, **41**, 163–194.

Eckart, C., 1948. An analysis of the stirring and mixing processes in incompressible fluids. *J. Mar. Res.*, **7**, 265–275.

Fisher, H. B., E. J. List, Koh R. C. Y., J. Imberger, and N. H. Brooks, 1979. *Mixing in Inland and Coastal Waters.* Academic Press, Inc., San Diego, CA.

Flierl, G. F., 1978. Models of vertical structure and the calibration of two-layer models. *Dyn. Atmos. and Oceans*, **2**, 341–381.

Freeland, H. J., P. B. Rhines, and T. Rossby, 1975. Statistical observations of the trajectories of neutrally buoyant floats in the North Atlantic. *J. Mar. Sci.*, **33**, 383–404.

Garrett, C., 1983. On the initial streakiness of a dispersing tracer in two- and three-dimensional turbulence. *Dyn. Atmos. and Oceans*, **7**, 265–277.

Haidvogel, D. B. and T. Keffer, 1984. Tracer dispersal by mid-ocean mesoscale eddies. Part I. Ensemble Statistics. *Dyn. Atmos. and Oceans*, **8**, 1–40.

Holloway, G. and S. S. Kristmannsson, 1984. Stirring and transport of tracer fields by geostrophic turbulence. *J. Fluid Mech.*, **141**, 27–50.

Ledwell, J. R., A. J. Watson, and C. S. Law, 1993. Evidence for slow mixing across the pycnocline from an open-ocean tracer-release experiment. *Nature*, **364**, 701–703.

Ledwell, J. R., T. Donoghue, J. Donoghue, and M. Sundermeyer, 1994. RV Seward Johnson cruise 9404, 10/11/94 - 4/12/94: Sampling cruise 6 - North Atlantic Tracer Release Experiment. Cruise report, Woods Hole Oceanographic Inst.

Maltrud, M. E. and G. K. Vallis, 1991. Energy spectra and coherent structures in forced two-dimensional and beta-plane turbulence. *J. Fluid Mech.*, **228**, 321–342.

Pedlosky, J., 1979. *Geophysical Fluid Dynamics.* Springer-Verlag, New York, N.Y.

Press, W. H., S. A. Teukolsky, W. T. Vetterling, and Flannery B. P., 1986. *Numerical Recipes.* Cambridge University Press, New York, N.Y.

Price, J. F. Particle dispersion in the western North Atlantic. Unpublished Manuscript, 1982.

Price, J. F., P. L. Richardson, C. M. Wooding, and M. E. Zemanovic, In preparation. The North Atlantic Tracer Release Experiment. SOFAR float data summary. Technical report, Woods Hole Oceanographic Inst.

Rhines, P. B., 1975. Waves and turbulence on a beta-plane. *J. Fluid Mech.*, **69**, 417–443.

Rhines, P. B., 1977. *The Sea*, chapter 7. The Dynamics of Unsteady Currents. Ed. Goldberg, E. D., I. N. McCane, J. J. O'Brien, and J. H. Steele. Wiley, New York, N.Y.

Taylor, G. I., 1921. Diffusion by continuous movements. *Proc. Lond. Math. Soc. A*, **20**, 196–212.

Trask, R. P. and N. J. Brink, 1993. WHOI Technical Report 93-12. Cruise report R/V Oceanus cruise # 240, leg 3. Subduction 1 Mooring Deployment Cruise, 17 June – 5 July, 1991. Cruise report, Woods Hole Oceanographic Inst.

Watson, A. J., K. Van Scoy, J. R. Ledwell, C. S. Law, Jones D., C. Marquette, T. Donoghue, S. Watts, M. I. Liddicoat, C. Fernandez, J. Bouthilette, D. Ciochetto, J. Donoghue, S. T. Bolmer, K. Tedesco, K. Smith, and J. Scott, 1993. RRS Charles Darwin cruise 78, 22/4/93 - 24/5/93: The North Atlantic Tracer Release Experiment - final sampling leg. Cruise report, Woods Hole Oceanographic Inst. and Plymouth Marine Lab.

Williams, R. T. and J. C-L. Chan, 1994. Numerical studies of the beta effect in tropical cyclone motion. Part II: Zonal mean flow effects. *J. Atmos. Sci.*, **51**, 1065–1076.

Young, W. R., P. B. Rhines, and J. R. Garrett, 1982. Shear-flow dispersion, internal waves and horizontal mixing in the ocean. *J. Phys. Oceanogr.*, **12**, 515–527.